Analysing and Predicting Chaos from Shocks and Radiative Cooling in Simulations of Cosmic Structure Formation

by

Paresh Mungara

A Thesis Submitted to Saint Mary's University, Halifax, Nova Scotia in Partial Fulfillment of the Requirements for the Degree of Master of Science in Astronomy (Department of Astronomy and Physics)

November 20, 2020, Halifax, Nova Scotia

Approved: _____

Dr. Robert Thacker

Approved: _____

Dr. Ian Short

Approved: _____

Dr. Luigi Gallo

Acknowledgements

I cannot express my gratitude enough for my supervisor, Dr. Robert Thacker, who has been an incredible advisor. It was his guidance and support that got me through every hurdle I encountered throughout the program. I would also like to thank my committee members Dr. Ian Short and Dr. Luigi Gallo for their time and constructive feedback.

A huge thanks to my friends in the graduate program, especially Kamal, Angelo, Preet, and Adam who were always there for me and made my time here in Halifax and at Saint Mary's memorable. Thanks to my parents and sister who have also provided a great deal of support, even though they were thousands of miles away.

Contents

List of Figures

List of Tables

Abstract

Analysing and Predicting Chaos from Shocks and Radiative Cooling in Simulations of Cosmic Structure Formation

by Paresh Mungara

It has long been appreciated that galaxy formation involves physics that can be subject to chaos. Numerical simulations introduce an additional source of noise in the form of approximations and floating point arithmetic errors. To date, there have been preliminary investigations into quantifying and characterizing the effects of both physical and numerical factors on simulation results, however, focusing on individual physical processes, such as shocks or radiative cooling, has been somewhat overlooked. In this thesis, we provide an analysis of the impact of shocks and radiative cooling in simulations of cosmic structure formation, by investigating a combination of phase space separation and density-phase space correlation. We have turned off other processes, such as star formation and feedback, to be able to focus on hydrodynamics with cooling alone. We find that regardless of cooling, galaxy mergers exhibit chaotic properties, however, cooling enables faster and stronger response to small initial changes. An initial hypothesis that high density regions should be more chaotic than low density regions is also shown to breakdown, especially at later times during the merger. Overall the development of differences in solutions is complex and involves distinct physical processes as well as mass scales.

November 20, 2020

Chapter 1

Introduction

Galaxy formation has been a topic of interest ever since we have become cognizant of their existence. Simulations of galaxy formation arguably started in the 1970s, with some of the pioneering work done by Dzyuba & Yakubov (1970), Toomre & Toomre (1972), Gott (1973, 1975), Larson (1974a,b, 1975, 1976), Miller (1978), Miller & Smith (1979a,b), Hohl & Zang (1979). However, in the last two decades computing technology has taken remarkable strides, allowing us to delve even further into the study of galaxy formation and evolution via the use of simulations. Numerical simulations have been, and continue to be, a vital tool which we use to help understand the formation of large scale structure of the universe. Simulations are often instrumental in testing theories against observational results, and thus hold a great deal of importance in the field. However, this predictive power must be critically assessed if we are to connect theory and observation via inference. This study is a step in the direction of analyzing the reliability and robustness of our simulation methods.

1.1 Overview of Galaxy Formation

Developing an understanding of galaxy formation has involved an interplay between theory and observation. Galaxies were identified to have either elliptical or a spiral shape in the 1920s (Hubble 1926), however, the models of formation of these structures were yet to be developed. Eggen et al. (1962) proposed a model which suggested that gas clouds collapsing due to gravitational instability form galaxies and the rate at which star formation happens determine whether the end product will be an elliptical or a spiral. If stars form rapidly, consuming most of the gas, the infall motions are converted into random motions, resulting in an elliptical galaxy. Alternatively, if star formation is slow, the cloud remains gaseous, making it easier for gravitational energy to be dissipated by means of shocks and radiative cooling. In this case, the cloud will continue shrinking until it is supported by angular momentum resulting in what resembles a disk shaped spiral galaxy. This idea was later extended by Gott & Thuan (1976) who argued that the amount of dissipation during the collapse depends on the amplitude of the initial density perturbation. Using a parameterization of star formation based on Schmidt (1959), they argued that larger initial perturbation in density leads to more rapid star formation, resulting in an elliptical galaxy and vice versa. The role of dark matter in galaxies was not yet appreciated in these early works, but it would later follow as an observational understanding of both the clustering of galaxies and dynamics within galaxies, grew.

The early theoretical development of galaxy formation was helped by the simultaneous growth of the ability to simulate galactic dynamics and evolution. Toomre & Toomre (1972)

used simple numerical simulations to demonstrate that some of the observed features in peculiar galaxies such as long tails could be explained by the interaction of two spiral galaxies. In this famous paper they argued that most elliptical galaxies could be remnants. This paved way to the currently accepted view (e.g. Mo et al. 2010) that most star formation happens in disk shaped spiral galaxies and high mass elliptical galaxies form through mergers of smaller galaxies, also known as hierarchical mergers. This notion is well supported by even early simulations of merging galaxies (White 1978; Gerhard 1981; Barnes 1988; Farouki & Shapiro 1982) exhibiting density profiles of the merged product closely matching that of observed ellipticals.

By the end of the 1970s it was becoming increasingly clear that a massive dark component was dominating galactic dynamics and the discovery of anomalous galaxy rotation curves by Rubin & Ford (1970) was, arguably, the single most important evidence for the existence of dark matter. The observational evidence suggested galaxies reside in massive dark halos that reach far beyond the baryonic extents. White & Rees (1978) proposed a theory, which underpins modern models, that dark matter halos form first through hierarchical clustering and gas cools and condenses in the gravitational potential of these dark matter halos, forming the stellar populations that we observe. However, their model predicts far more faint galaxies than observed, but adopting the cold dark matter scenario produces an increased number of faint galaxies at high redshifts (Blumenthal et al. 1984). The White and Rees framework can solve some of the problems arising from older models, for example, it was argued by Efstathiou & Silk (1983) that without dark matter, gas cooling down to form a rotationally supported disk will take substantially longer than a small fraction of the Hubble time. It

was also argued that extended dark matter halos allow for a higher probability of a merger event which was a requirement for Toomre & Toomre (1972) model of hierarchical mergers.

The theoretical development of galaxy formation has accelerated greatly since the mid 1990s. Structure formation with Cold Dark Matter has been extensively studied (see Benson 2010 for a review) both through semi-analytical models and hydrodynamical simulations. Semi-analytical modelling (SAM) involves constructing a set of coherent analytic approximations for the physical processes involved in galaxy formation. Within the realm of simulations, low and high resolution studies with complex physical models such as supernova feedback, AGN feedback, star formation have been performed (Thacker & Couchman 2000; Kay et al. 2002; Marri & White 2003; Stinson et al. 2006; Cox et al. 2006; Scannapieco et al. 2006; Tasker & Bryan 2006; Booth & Schaye 2009; Hopkins et al. 2014; McCarthy et al. 2017; Park et al. 2017; Moreno et al. 2020). Low resolution simulations, typically with a few thousand resolution elements per object, allow the probing of statistical questions about galaxy formation (Marri & White 2003; Bourne et al. 2015; Lupi et al. 2017), while higher resolution simulations, with number of resolution elements on the order of millions, probe specifics of the individual processes involved in galaxy formation (Green & van den Bosch 2019; Kimock et al. 2020; Hopkins et al. 2020) The combination of these two techniques have allowed us to develop a comprehensive understanding of how galaxies form and evolve.

However, a number of recent studies of galaxy formation indicate (Keller et al. 2019; van den Bosch & Ogiya 2018; Su et al. 2018) that it is a chaotic process and predicting the precise nature of the chaos which governs these events is crucial to understanding the statistical and systematic variation of results. This realization is an important step toward

making galaxy formation a more strongly predictive science.

1.2 Chaos

There are dynamical systems which have integrable equations of motion, such as the two body system governed by inverse square force law, which can be integrated to find an exact form solution. However, for many systems, an exact solution does not exist. Such systems may have potentials that can be divided into an integrable part and an additional weaker term which might couple variables together to make them inseparable. This coupling makes the equations of motion unintegrable. If the additional term is significantly weaker than its integrable counterpart, it could be solved with classical perturbation theory, but if it is not, we have to solve the equations in their entirety without any approximations. Such systems need to have their evolution solved numerically.

The solutions can be well behaved, in the sense that small changes in initial conditions will result in a small change at a later time. However, a system is considered chaotic if a small change in its initial conditions will result in a large change in the final state.

To discuss this issue further, we re-cap the definition of a dynamical system's phase space. A system with N degrees of freedom spans a $2N$ dimensional "phase space" in position and momentum. For example a single particle 3D system will have a six-dimensional phase space, three for positions (x, y, z) and three for momenta (p_x, p_y, p_z). The trajectories in the phase space of a multi-component system can be very complex and conceptually impossible to follow in a large number of dimensions. Thus a section in the phase space which is of

reduced dimensions (specifically two), called *Poincaré section*, can be used to gain insight. The behaviour of the system can be inferred from the behaviour of phase space trajectories on these sections (see section 11.5 in Goldstein et al. 2002 for more information on Poincaré sections). Such an approach was used in the classic Henon & Heiles (1964) study of chaos in galactic dynamics.

For systems that undergo chaotic behaviour, characterized by rapidly diverging paths in phase space, we utilize the Lyapunov exponent, usually denoted λ, to classify their behaviour. Two systems separated by an infinitesimally small distance δX_0 in phase space, will experience an exponential growth in their phase space separation $X(t)$ according to,

$$X(t) = e^{\lambda t} \delta X_0 \tag{1.1}$$

The inverse of λ defines the characteristic e-folding time for the divergence of chaotic trajectories. Technically the large number of dimensions of phase space mean that there is not just a single Lyapunov exponent, there is in fact an entire spectrum of them corresponding to the different axes of phase space. In practice, the evolution of systems is frequently discussed in the context of a single Lyapunov exponent.

1.2.1 Hamiltonian and Non-Hamiltonian Chaos

There are mainly two types of chaos which are separated by their behaviors in the phase space, Hamiltonian and non-Hamiltonian. Hamiltonian systems have a fundamental property addressed by Liouville's theorem, that the phase space volume is conserved throughout

the time evolution. This gives rise to the fact that there are no "attractors", meaning, for any given initial condition the system does not converge to a common time-evolving state, i.e. all the systems follow their own specific solutions. Non-Hamiltonian chaos on the other hand is exhibited by systems that have input or dissipation of energy, a consequence of which is the potential existence of attractors. There could be fixed point attractors such as the rest state of a simple pendulum in the presence of a dampening force, or something called strange attractors such as the Lorenz attractor.

To put this into the perspective of galaxy formation, one needs to be first aware that the dark matter halo alone is a Hamiltonian system which evolves under gravity. If gas is present in the system, there are coupled interactions between gas and dark matter which create a possibility of (periods of) non-Hamiltonian chaos if cooling and heating are allowed. These systems could eventually reach a low energy stability since energy is being taken out of the system, unless heating is also allowed. Of course the precise nature of any end point depends on how material cools within the dark matter halo and the dynamics of the halo. In nature the situation is more complex as cooled material becomes stellar and is cycled into the ISM over time. But, overall, the concept of dissipation is analogous to a simple pendulum operating under a drag force which evolves towards a stable (stationary) equilibrium unless it is also being driven by another external force. It is important to understand that a pendulum loses energy and angular momentum while a galaxy continues to rotate around the centre even when gas clouds dissipate energy, thus these systems are different in that regard. This study focuses primarily on the effects of cooling on galaxy formation and subsequent evolution which is why non-Hamiltonian chaos is of particular importance.

Galaxy formation has been known to exhibit irreversible chaotic behavior for decades (Miller 1964; Kandrup & Smith 1991). It has generally been regarded as unimportant in the evolution of global galaxy properties, but it limits our predictive ability as shown by Keller et al. (2019). They showed that this chaotic behavior cannot be overcome by more sophisticated algorithms or higher resolution as it is a fundamental feature of the underlying physics. To make matters worse, additional discreteness noise and floating point arithmetic errors are added by numerical simulations which could potentially be amplified by physics. Building a better understanding of this issue, as it cannot be removed, is a critical step towards making robust comparisons of simulations and observations.

1.2.2 Discreteness Noise

The time taken by a typical dynamical object to change its energy to the mean energy of the system by means of dynamical encounters is known as the relaxation time. In a galaxy, this timescale is significantly longer than the age of the universe, which implies close encounters are unimportant to the galactic systems we observe. Due to this, we can consider a galaxy a collisionless system. For this reason, while simulating galaxies, individual encounters are ignored (or avoided, by means of softening length) and stars react to a smooth potential generated by the rest of the system, which is approximated as a continuous distribution (Hernquist et al. 1993). By using a necessarily limited number of particles to sample a continuous density function, we are subjected to discreteness noise, which is on the order of $\frac{1}{\sqrt{N}}$ (van den Bosch & Ogiya 2018). We could always increase the number of particles until it matches that of a real galaxy, but even then discreteness noise will have some effect,

albeit less, and one can argue it is not clear that we know what the level of discreteness in the dark matter distribution is. Exceptional progress has already been made, from using a few hundred particles just a few decades ago (Toomre & Toomre 1972) to upwards of a million particles to even a billion particles at the present (van den Bosch & Ogiya 2018; Springel et al. 2008), but we are still far from reality where galaxies typically have billions to hundreds of billions of stars.

1.2.3 Floating-Point Arithmetic

Another significant potential point of concerns comes from floating point arithmetic. Floating point operations done on a computer are not associative meaning, $(a+b)+c \neq a+(b+c)$. This arises from the fact that, nominally, infinitely precise numbers are represented on a computer with finite precision *i.e.* numbers are "rounded-off" to the precision of the computer. This may seem trivial as double precision round off errors are on the order of one part in 10^{15}, however if a system shows strongly chaotic behaviour, these minute differences can cause the system to diverge in phase space quickly. This means that changing something as simple as the order of operations can drastically change the final state of the system.

Reduction operations in parallel computing, which utilize the associative property of operations such as summation to reduce a problem to a smaller subset so that it could be run in parallel, are non-deterministic (He & Ding 2001). Subtle variations in processes on machines running in parallel can introduce round-off errors and unfortunately we currently do not have algorithms to combat this issue other than some that are still in experimental stage (Balaji & Kimpe 2013). Even if these reduction operations could be avoided, simu-

lations have checkpoints where the current state of the system is dumped so that it could be restarted at a later time in case of a hardware failure or any other reason. If these checkpoints are used to restart simulations, the order of operations could be changed leading to a diverged solutions (Keller et al. 2019). While some programmers (e.g. GIZMO by Hopkins (2015)) have gone to significant lengths to ensure on a set number of processors the accumulations happen the same way as opposed to dynamic load balancing systems, in practice this is essentially hiding the issue. The results are no more accurate whether a sum is performed forwards or backwards or in some other order.

1.3 Overview of Simulation Methods

Following an actual galaxy's entire evolutionary path is not possible due to the timescales involved, however, observing a population gives us a better idea of how they evolve in an ensemble context. Wide field galaxy surveys like Sloan Digital Sky Survey (SDSS, York et al. (2000)) aim to do just that. By using surveys like these, we can study galaxies at various evolutionary phases to construct a picture of how galaxies might evolve. However, there are still many gaps that can not be filled, such as short timescale properties in addition to the possibility that individual galaxies within the ensemble do not follow averaged behaviours (the ecological fallacy). To help bridge this gap between theory and observations, numerical simulations are helpful. Here we provide a brief overview of the methods used to simulate dark matter and baryons.

1.3.1 Gravity

The main challenge for numerical simulations is to calculate the gravitational force acting upon a mass element from all the other particles. This is accomplished by solving the Poisson's equation, or using Newton's law of gravitation by calculating forces on particles by each and every other particle which is very computationally intensive. N-body codes or gravity solvers are divided into three groups by the way they approach solving the Poisson equation, particle-particle based, particle-mesh based, or the Hybrid of the two. Particle-particle (PP) approach aims to solve the integral form of the Poisson's equation,

$$\mathbf{\Phi}(\mathbf{r}) = -G \int \frac{\mathrm{d}\mathbf{r}' \, \rho\left(\mathbf{r}'\right)}{|\mathbf{r} - \mathbf{r}'|} \tag{1.2}$$

where Φ is the gravitational potential and ρ is the matter density. A popular particle-particle approach is the tree approach as outlined by Barnes & Hut (1986). Earlier simulations employed a direct summation brute-force $\mathcal{O}(\mathcal{N}^2)$ calculation to get the gravitational potential but the tree code approximates the forces from distant particles by Taylor expanding the force, making it a faster $\mathcal{O}(\mathcal{N} \log \mathcal{N})$ algorithm.

The second approach is the particle-mesh (PM) method which solves the differential form of the Poisson's equation,

$$\nabla^2 \mathbf{\Phi}(\mathbf{r}) = 4\pi G \rho(\mathbf{r}) \tag{1.3}$$

through fast Fourier transform-based methods with Poisson's equation in Fourier space. The PM method computes the potential on a grid via a Fourier transform of the density

field and moves particles along potential gradients (Hockney & Eastwood 1988; Somerville & Davé 2015). Particles do not directly interact with each other but only through a mean field. This method softens the interaction of scales smaller than the grid cell length.

Hybrid schemes combine the two approaches outlined by using direct summation techniques for short range interactions and Fourier transform based approaches for long range interactions. This scheme is more powerful because it utilizes the ability of PP techniques to accurately represent forces down to the softening length which is important in high density regions.

1.3.2 Hydrodynamics

In order to model the baryonic content of galaxies, we need to solve hydrodynamical equations and gravity simultaneously. This matter is approximated as a non-relativistic ideal gas and is usually evolved by solving the Euler equations (a form of Navier-Stokes equations with no viscosity or conduction) which represent mass, energy and momentum conservation. Depending on whether one uses advective or partial derivatives, these equations can be expressed in different forms leading to different schemes of solving them, which essentially fall into two classes, Langrangian and Eulerian (Vogelsberger et al. 2020).

The main difference between Lagrangian and Eulerian approaches is the frame in which the Euler equations are solved. Lagrangian methods utilize the fluid frame as opposed to the fixed frame of Eulerian approaches (Somerville & Davé 2015). The latter discretize the fluid onto grid cells, computing the advection of properties such as energy and momentum across the cell walls. Lagrangian methods, on the other hand, have particles (or fluid elements)

themselves carry all the information about the fluid. A popular Lagrangian approach is Smoothed Particle Hydrodynamics (Gingold & Monaghan 1977; Lucy 1977), which has influenced much astrophysical simulation of galaxy formation. There are advantages and disadvantages to either Lagrangian or Eulerian approaches, thus there is growing interest in hybrid techniques that remove drawbacks of either method. AREPO (Springel 2010) for example uses an arbitrary Lagrangian-Eulerian method and is able to naturally follow the fluid as in a Lagrangian code, while also maintaining advantages such as shock handling provided by Eulerian codes. Excellent summaries of all the simulation methods currently in use and in development have been provided by Somerville & Davé (2015) and more recently by Vogelsberger et al. (2020).

1.4 Motivations for this study

There have been a number of studies of chaos in galaxy formation (Keller et al. 2019; van den Bosch & Ogiya 2018; Genel et al. 2019; Su et al. 2018) focusing on numerical factors as well as physical processes. However, given the inherent complexity of these processes and their potential to drive small scale variations to very large scales, it is important to try to develop an understanding of the contributions of each individual process rather than simply running simulations and presenting measured variations. We would naturally tend to expect that the more processes are included in a simulation the more difficult it is to disentangle individual contributions. The motivation for our approach stems largely from this concern. Thus we chose to run simple and idealized galaxy merger simulations which instead of having

a multiplicity of physical models and initial conditions, focus on single cases and physics. Beyond adiabatic gas dynamics, radiative cooling was a natural additional piece of physics to include in our analysis. Being a precursor to a myriad of processes such as star formation and eventually stellar feedback, it is highly important from a phenomenological perspective.

However, even without cooling, a hydrodynamic system can exhibit behaviours of a chaotic system. With the addition of a cooling term, the evolution of the internal energy of the gas becomes difficult to integrate given the sensitive dependence of the cooling rate on temperature, as shown in Figure 1.1. This makes the overall evolution of the system challenging to follow since modern codes, including GIZMO are only first order accurate in taking cooling steps while being second order accurate in time and space (Zhu et al. 2017). Considering these facts, we can presume that we are losing precision faster when cooling is included. This would manifest beyond the temperature of the gas as that directly impacts both positional and momentum information. In the most extreme cases the position and momentum phase spaces of two nearly identical galaxies would follow diverging trajectories which could be characterized as chaos. It is also important to remember that there are larger differences than phase space evolution alone, as noted, we are not explicitly following the internal energy degree of freedom in these assessments and that could also show different behaviours.

It is important to emphasize that while we will refer to phase space evolution we are often referring either to particle-particle level variations (i.e. sub-spaces of phase space) or the phase space of the gas alone. To be clear, we accept that the gas phase space is an arbitrary construct as it ignores the dark matter which heavily influences the overall evolution of the

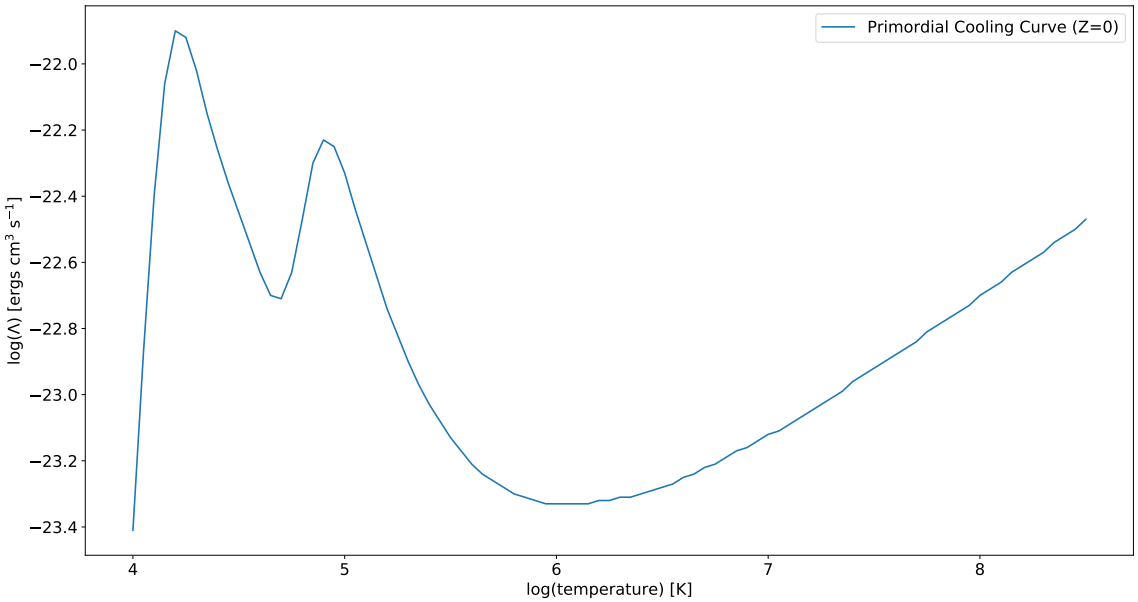

Figure 1.1: The primordial (metal-free) cooling function for gas in collisional equilibrium. Plotted based on data from Sutherland & Dopita (1993). The first peak corresponds to collisional excitation and ionization of hydrogen, while the second peak corresponds to the same processes for helium. At high temperatures, cooling is dominated by free-free emission.

gas. However, as a method of understanding the distinct evolutionary tracks of systems it is a useful and informative construct even if it is not expected to show conservation behaviours associated with Hamiltonian systems.

Given our expectation that cooling affects the growth of variations, we might naturally expect that the regions with higher densities should be more susceptible to chaos than low density regions as cooling rates grow in proportion to the square of the density. If it does correlate with density then we have a simple measure of predicting how chaos evolves. Conversely, the long range nature of the gravitational force means that we may see transport of variation over large scales in the simulation. Hence to examine this expectation we were motivated to look at the correlation of density with the phase space separation, specifically

measured in particle sub-spaces, between two runs with nearly identical initial conditions.

This thesis is organized as follows. In Chapter 2, we explore the code used for this study, the initial conditions and include information on all of the simulations we performed. In Chapter 3 we present the results of our simulations which are further discussed in Chapter 4. Finally, we conclude the thesis and briefly discuss future work in Chapter 5. In Appendix A we will present a brief analysis on the impact of changing the gravitational softening length used to reduce the impact of short-range two-body interactions.

Chapter 2

Simulation Methods

2.1 Simulation code: GIZMO

GIZMO (Hopkins 2015, based on earlier work by Springel 2005) was used for this study. GIZMO is a massively parallel code for N-body and hydrodynamical systems which includes a number of physics modules beyond hydrodynamics and gravitational physics. It includes various hydrodynamical methods, such as several types of Smoothed Particle Hydrodynamics (SPH), more advanced Lagrangian methods, Eulerian fixed-grid schemes, and also subgrid physics modules for AGN and supernova feedback, star formation and more.

2.1.1 Hydrodynamic Solver

A large number of hydrodynamic simulation codes used to simulate galaxy formation have relied upon the SPH approach. The SPH method uses discretized particles to represent a continuous fluid and interpolates hydrodynamic quantities, such as density, at any given

point in space. Effectively, this means that the density of a fluid at a given point is a weighted sum over nearby particles. Each particle has an associated smoothing length which is set according to the number of nearest neighbours used. While used extensively as a simulation tool, the SPH method is known to have limitations such as "oversmoothing" of shocks and poor representation of contact discontinuities. Because shocks are a potential carrier of small scale variations to much larger scales it is important that this process be modelled well.

GIZMO, along with options to choose from a multitude of SPH implementations, introduced a new hydrodynamic solver called the Lagrangian Meshless Finite-Mass (MFM) method. It is important to note that although MFM is a Lagrangian method like SPH, they are quite different in many respects. A particularly useful advantage of MFM over SPH is that it is a shock-capturing method. In shock-capturing methods, discontinuities are computed as part of the solution unlike shock-fitting methods where shocks are treated specially, or artificial viscosity methods which stabilize numerical techniques around shocks. MFM achieves this by dividing up the cell volumes associated with each particle used to calculate hydrodynamic quantities, this concept is similar to the Voronoi tessellation. Each point in space has an associated volume, unlike SPH where points relate to a number of smoothed particles based on the spherical kernels. In summary, MFM is a modern algorithm which outperforms SPH in many of the problems in numerical hydrodynamics (see Hopkins 2015, for detailed comparisons) and was thus the tool of choice for this study.

2.1.2 Radiative Cooling and Pressure Floor

Radiative cooling is central to this investigation and was the only additional fluid physics included in the simulations. The standard cooling module in GIZMO assumes optically thin cooling via atomic processes. It includes cooling and heating from hydrogen and helium ionization[1], recombination[2], free-free[3], and Compton effects such as scattering[4]. The cooling rates extend from $\sim 10^4$ K to 10^9 K. Ionization and recombination requires an assumption for the UV background, but since star formation is turned off, it is not required. There are additional cooling processes available within GIZMO such as fine-structure, metal line and molecular, but in the absence of star formation or feedback which we are not including for the purposes of examining simpler behaviours, we cannot motivate including these processes. For detailed descriptions of all the cooling physics and fitting functions, refer to Hopkins et al. (2018).

Including radiative cooling in galaxy simulations results in cool cores forming at the centre of halos. Without sufficient heating, cooling is dominant and these cool cores become unphysically dense (H_2 densities of $\sim$500 cm^{-3} as compared to $\sim$100 cm^{-3} in a typical giant molecular cloud.), while in our universe star formation leads to feedback that reheats collapsing gas. Within a simulation with such high densities, errors occurring from discretization, as mentioned in section 1.2.2, play a key role in artificial fragmentation of the gas. In essence, as gas cools below the Jeans temperature, the system can artificially frag-

[1]Free electron collisionally excites a bound electron which decays releasing a photon.
[2]Free electron recombining with an ion radiating away its kinetic energy.
[3]Free electron when accelerated by an ion, releases a photon; Also known as Bremsstrahlung
[4]Electron loses energy after colliding with a photon, by a process known as Inverse Compton Scattering.

ment (Bate & Burkert 1997; Truelove et al. 1997). For the purposes of this study, since we are focusing on classifying chaos and star formation is turned off, the precise nature of this fragmentation is actually unimportant. However, higher densities demand shorter integration time-steps, so much so that in many cases that it would take an exceptionally long period of CPU-time to evolve the system for a even a few million years. As a compromise, a density dependent artificial pressure floor was added to the simulations. In this method, implemented in GIZMO according to Robertson & Kravtsov (2008), an artificial pressure term is added to the equations of motion which counteracts gravitational collapse at high densities where the Jeans length is smaller than the resolution limit. This allows for longer time-steps and thus a shorter simulation time. From a theoretical perspective this approach has sometimes been seen as a crude form of feedback, but for the purposes of this study that analogy is not relevant.

2.2 Initial Conditions

Initial halos consisting of dark matter were generated using GalactICS (Galaxy Initial ConditionS; Kuijken & Dubinski 1995; Widrow & Dubinski 2005; Widrow et al. 2008) with the NFW density profile. A modified version of GalacICS developed by Thompson (2017) was used to insert gas in hydrostatic equilibrium with a temperature profile according to Kaufmann et al. (2007), in a spherical configuration within the dark matter halos. The gas then

follows density and temperature profiles according to,

$$\rho_G(r) = \rho_0 \left[1 + \left(\frac{r}{r_c}\right)^2\right]^{-1.5\beta} \tag{2.1}$$

$$T_G(r) = \frac{\mu}{k_{\rm B}} \frac{1}{\rho_G(r)} \int_r^\infty \rho_G(r) \frac{GM_{\rm tot}(r)}{r^2} {\rm d}r \tag{2.2}$$

where r_c is the core radius, β is the outer-slope parameter, μ is the mean molecular weight, k_B is the Boltzmann constant, ρ_G is the gas density, and $M_{\rm tot}$ is the total mass (dark matter and gas). The gas density profile is an observationally motivated β-profile (e.g. Cavaliere & Fusco-Femiano (1976))

The way in which the gas particles are distributed in the above mentioned configuration is as follows: First the volume is divided into spherical shells of equal mass (based on Equation 2.1) which are then populated according to the density profile such that each shell has an equal number of particles at random positions. Temperatures to be assigned to gas particles were calculated by first creating equal width spherical bins and calculating masses and densities in these bins to get the radial terms in Equation 2.2. Once these quantities are known, the temperature integral is simply approximated as a summation to get the final temperature for a given particle.

Since dark matter distributions were scaled rather than recomputed at different masses, parameters such as the radius, radial velocity dispersion were scaled according to a base configuration from Thompson (2017) to get four halos of total masses ranging from 8.4×10^{10} to 8.45×10^{13} $M_\odot$. For the merger, an identical halo and gas copy was placed such that the

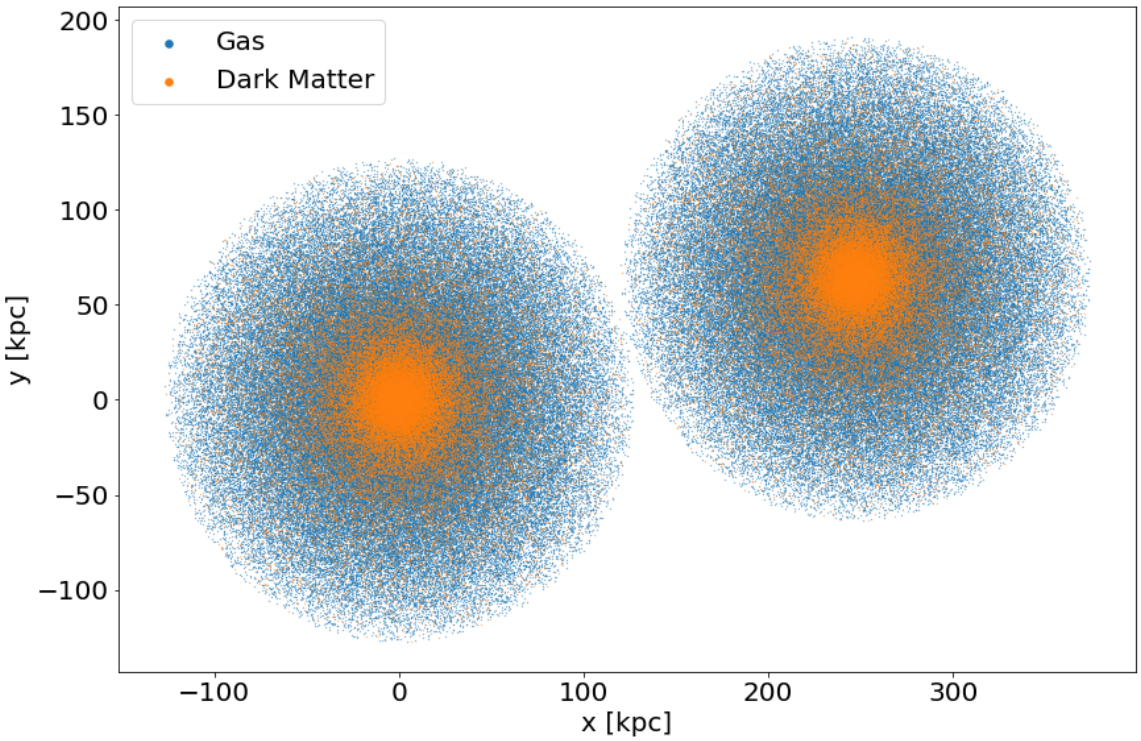

Figure 2.1: The x-y projection of the initial conditions snapshot for the lowest mass halos ($8.4 \times 10^{10} M_{\odot}$)

distance between their centres is twice the radius, as shown in Figure 2.1. We explored two merger scenarios, one where the second halo is on a parabolic trajectory towards the first one and one where they collide via freefall from no initial movement. For the former, the initial velocity boost was calculated for the halo as a whole and every particle was assigned this velocity boost. The boost was calculated by fixing the periapsis[5] to match Mihos & Hernquist (1996), a choice used extensively in merger simulations. The dark matter particles were given an additional rotational velocity to simulate a typical halo with spin parameter[6]

[5]Periapsis is the closest distance between two objects on an orbit.

[6]Spin parameter is generally denoted by λ in the literature but to avoid confusion with the Lyapunov exponent, it is denoted as λ_0

$\lambda_0 \sim 0.05$ calculated using,

$$\lambda_0 = \frac{J|E|^{\frac{1}{2}}}{GM^{\frac{5}{2}}} \tag{2.3}$$

where J is the angular momentum, E total energy, and M total mass. Gas particles were not given any rotational velocity. Despite the addition of this halo spin, it is worth emphasizing that the dominant angular momentum component is in the orbital angular momentum of the parabolic merger, while the head on merger has distinctly less overall angular momentum. Freefall runs have 55% less angular momentum than parabolic runs. Choosing these two scenarios allows us to see how overall dynamics potentially impacts results.

Once these initial conditions were set-up it was necessary for us to also create perturbed initial conditions, which would be used for the "shadow" simulation, to be able to follow the divergence of evolution. Hence, we generated a suite of initial conditions identical to the previous one except a minor modification in the position of one of the particles. We specifically focused on the gas particles in this case, and our fiducial choice is to move a gas particle closest to the centre of one of the halos halfway towards the nearest gas particle. These shadow simulations represent a different point in the phase space very close to their respective originals. Strictly speaking a full analysis of the phase space separations would involve running simulations where each particle was moved, essentially the full *Lyapunov Spectrum*. However, due to our limited computational resources we considered an additional set of initial conditions for our lowest mass system. This simulation consists of the particle located at half mass radius (HMR) and at the edge of the halo. A detailed description of all the initial conditions is given in Table 2.1.

We also estimate the cooling times for the generated galaxies based the primordial cooling curve as shown in Figure 1.1. The expression used is as follows,

$$\mathrm{t_{cool}} = \frac{E}{\frac{\mathrm{d}E}{\mathrm{d}T}} = \frac{\frac{3}{2}nk_BT}{n^2\Lambda(T)} \tag{2.4}$$

where n is the particle density, T is the temperature and $\Lambda(T)$ is the cooling rate at temperature (T). Cooling times in the central regions and the average for the entire distribution, using virial temperature and density, are given in Table 2.2. It is worth noting these are only approximations and a more rigorous procedure would include integrating over the variation in density as the system cools as well as the change in cooling rate with lowering temperature. Consequently, the values only give the reader a rough idea of comparative cooling times even if this approach is used extensively in the literature.

The total number of particles for each simulation is kept roughly similar. Small differences arise as a product of repeating the temperature calculation since as the radial distances change so does the binning, leading to very slightly different numbers of particles. We choose to keep the softening lengths[7] (ϵ) a fixed fraction of the inter-particle spacing, so they scale in proportion to the cube root of the mass ratio of one halo to another. Virial radii (R) naturally grow as the cube root of the mass ratio as well. The ratio of dark matter to baryon mass is set to 5 to closely match the most recent measurement of the proportion of dark matter to baryons ΛCDM cosmology (Ibarra 2015), although since there are no cosmological

[7]Softening is a modification applied to the gravitational potential so that it does not diverge as the particles get closer. It can also be thought of as a spatial resolution where forces below the softening length (ϵ) are smoothed. The value of the softening length is dependent on the objective of the simulation and computational resources, however, there are studies (e.g. Zhang et al. (2019)) that argue for an optimal softening length by parameterizing it using the number of particles and virial radius.

Table 2.1: Parameters for the initial conditions where halos are in parabolic and freefall trajectory collisions. M: Mass of individual halos, n: number of particles, m: mass of each particle, ϵ: Softening Length, R: radius, q: periapsis (only for parabolic trajectory runs), HMR: half mass radius. For each case, there is a shadow initial condition which is identical to its counterpart except the perturbation in one of the particle's position.

M $[M_\odot]$	$n_{\mathbf{gas}}$	$m_{\mathbf{gas}}$ $[M_\odot]$	$\epsilon_{\mathbf{gas}}$ **[kpc]**	$n_{\mathbf{DM}}$	$m_{\mathbf{DM}}$ $[M_\odot]$	$\epsilon_{\mathbf{DM}}$ **[kpc]**	**R** **[kpc]**	**q** **[kpc]**	**Location of Modified Particle**
8.40×10^{10}	193002	7.19×10^4	0.093	49334	1.41×10^6	0.464	127.64	4.06	centre
									HMR
									Edge
8.41×10^{11}	193327	7.21×10^5	0.200	49365	1.41×10^7	1.000	275.00	8.75	centre
8.42×10^{12}	193956	7.19×10^6	0.431	49381	1.41×10^8	2.154	592.47	18.85	centre
8.45×10^{13}	195068	7.15×10^7	0.928	49396	1.41×10^9	4.642	1276.44	40.61	centre

Table 2.2: Cooling times for the galaxies used in our simulations. Λ is the cooling rate at a given temperature. Refer to Figure 1.1 for the cooling curve.

Mass $[M_\odot]$	**Virial Densitiy** $\left[\frac{1}{cm^3}\right]$	**Virial Temp [K]**	**Λ at Virial Temp** [ergs cm^3 s^{-1}]	**Central Density** $\left[\frac{1}{cm^3}\right]$	**Central Temp [K]**	**Λ at Central Temp** [ergs cm^3 s^{-1}]
8.40×10^{10}	3.22×10^{-4}	1.68×10^{5}	1.67×10^{-23}	3.31×10^{-2}	2.20×10^{5}	1.10×10^{-23}
8.41×10^{11}	3.23×10^{-4}	7.80×10^{5}	4.80×10^{-24}	3.34×10^{-2}	1.10×10^{6}	4.68×10^{-24}
8.42×10^{12}	3.23×10^{-4}	3.63×10^{6}	5.42×10^{-24}	5.35×10^{-2}	4.92×10^{6}	5.98×10^{-24}
8.45×10^{13}	3.24×10^{-4}	1.69×10^{7}	9.14×10^{-24}	6.01×10^{-2}	2.29×10^{7}	1.04×10^{-23}

Mass $[M_\odot]$	**Central Region Cooling Time [Gyr]**	**Virial Cooling Time [Gyr]**
8.40×10^{10}	0.02	1.03
8.41×10^{11}	0.23	16.62
8.42×10^{12}	0.51	68.41
8.45×10^{13}	1.21	188.19

predictions in these simulations this choice is motivated more by consistency than precision.

2.2.1 Diagnostics of the Initial Conditions

A brief diagnostic review of the initial conditions is presented here. The density profile is derived from the commonly-used NFW profile with the truncation of dark matter performed using an error function,

$$\rho_{\rm dark}(r) = \frac{\rho_0}{(r/a_h)^{\gamma}\,(1+r/a_h)^{3-\gamma}} \left[\frac{1}{2}\,{\rm erfc}\left(\frac{r-r_h}{\sqrt{2}\delta r_h}\right)\right] \tag{2.5}$$

where r_h is the truncation radius and a_h is the break radius where the slope of the profile changes from -1 to -3. The gas is simply truncated at the radius of the dark matter halo. Measured density profiles for dark matter and gas are shown in Figure 2.2, using radial bins of 50 particles to assure modest bin variances. Because the base dark halo is generated from Thompson (2017) and GalactICS is scaled to other masses it is only necessary to review this configuration. For comparison we provide a best-fit model to the dark matter density which we find to be slightly different from the prescribed initial parameters, break radius $a_h = 14.7$ kpc from the fit compared to 13.6 kpc used to generate the halo, but since this is quite sensitive to the fit within the central region, where statistics are poorer, overall this demonstrates a physically plausible initial condition from a dark matter density perspective.

It is worth emphasizing that the state of the gas, as solely a hot sphere, is a significant approximation relative to gas within galaxies or within groups/clusters of galaxies at larger mass scales. However, by using essentially the same physical model at different mass scales

we can diagnose the differences that additional physics, such as temperature dependent cooling, introduces.

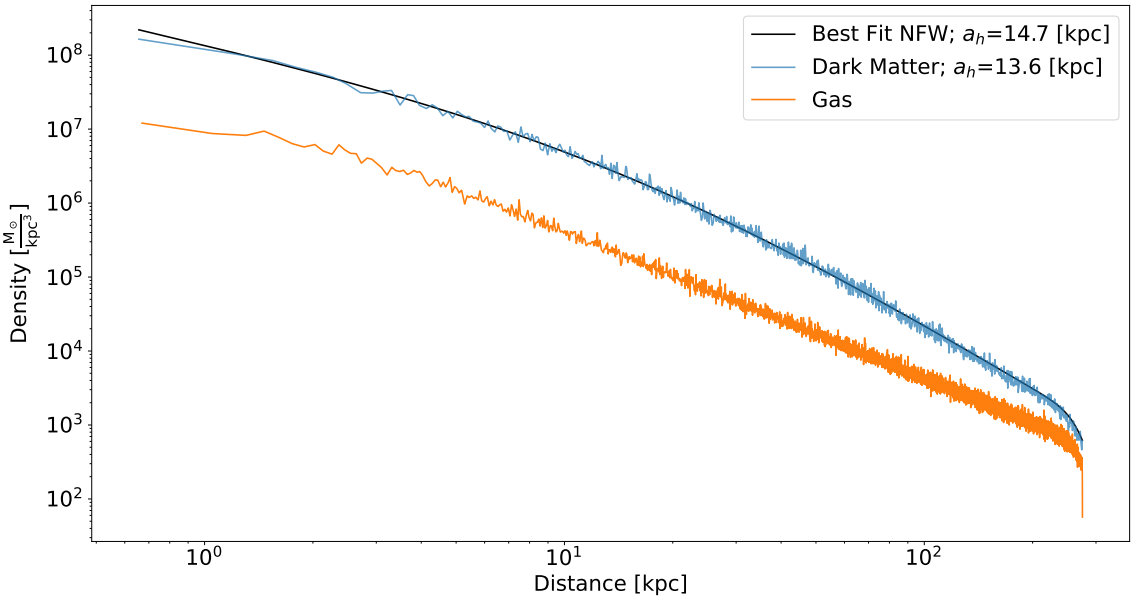

Figure 2.2: Initial gas and dark matter density profiles for the $8.41 \times 10^{11} M_\odot$ galaxy. Dark matter is modelled by the NFW profile (equation 2.5) and gas according to Equation 2.1. There is a slight discrepancy between the retrieved break radius a_h and the the same used to generate the halo.

In addition to the density profile we can review the circular velocity, and circular velocity profiles for the two lowest mass systems are shown in Figure 2.3. The two higher mass galaxies follow a similar profile out to their respective radii. The shape of the rotation curve is broadly similar to current observations (the rotation curve of Milky Way from Mróz et al. (2019) is shown in 2.3) although not quite as centrally peaked. This is consistent with the lack of a central concentration of mass.

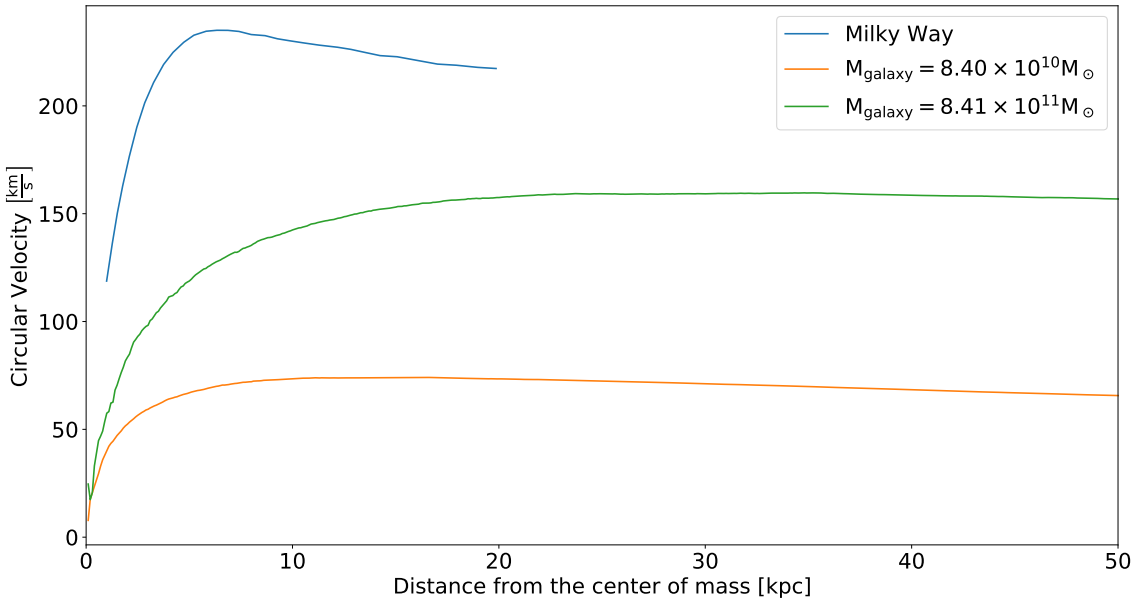

Figure 2.3: Initial circular velocity profiles for the two low mass galaxies in our simulations and for comparision, the Milky way by Mróz et al. (2019).

2.3 Simulation suite

In addition to the variation in evolution simulations without cooling, shocks being a key part of our concern there, we are also strongly motivated to investigate the impact cooling has on the phase space evolution during a galaxy merger. Since cooling is a function of temperature and density, different mass halos will cool at a varying rate. With atomic cooling processes active below 10^6 K that means the lowest mass halos will cool faster.

Thus we set up a suite of simulations that explore the same physical processes but with halo masses varying by factors of 10, details of which are provided in Tables 2.3 and 2.4. Each case has its shadow run where a particle's position is modified to be closer to its nearest neighbor as a potential seed for perturbation in the phase space. The location of this particle

is chosen to be at the centre of one of the two halos where the density is highest and is thus expected to have a larger impact eventually due to it undergoing more interactions than a particle in lower density region.

Runs are identified with the following schema: first two digits represent the order of magnitude for individual halo mass, next digit for cooling (1 : on, 0 : off) and finally a letter to describe their merger trajectory (p : parabolic, f : freefall). To avoid confusion, we emphasize that the pre-factor of 8 on the masses means that the total mass in the merger is in fact the next exponent higher, but we always refer to simulations via this lower exponent corresponding to the individual halo and gas system.

The next experiment was to explore the impact of the location of the perturbed particle. Two additional runs were performed with the perturbed particle located at half mass radius and at the edge of the distribution for the lowest mass halos. Cooling was turned off for these simulations to focus more closely on the contribution of the location of perturbation. Details for this suite are described in Table 2.5. Lastly, we performed three more simulations to study the effects of softening length and their details are given in Table 2.6.

Table 2.3: Descriptions of runs where the merging galaxies are on a parabolic trajectory including their ids for further referencing. **Note:** Due to time constraints and lack of angular momentum conservation, 101p and 111p were simulated for 3.13 and 7.73 Gyr respectively, while the rest were run for 9.78 Gyr.

Run Id	**Mass [$M_\odot$]**	**Cooling**	**Trajectory**	**Location of Perturbed Particle for the Shadow Run**
101p	8.40×10^{10}	On	Parabolic	centre
100p	8.40×10^{10}	Off	Parabolic	centre
111p	8.41×10^{11}	On	Parabolic	centre
110p	8.41×10^{11}	Off	Parabolic	centre
121p	8.42×10^{12}	On	Parabolic	centre
120p	8.42×10^{12}	Off	Parabolic	centre
131p	8.45×10^{13}	On	Parabolic	centre
130p	8.45×10^{13}	Off	Parabolic	centre

Table 2.4: Descriptions of runs where the merging galaxies are in a freefall including their ids for further referencing. **Note:** Due to time constraints, 101f, 111f, and 121f were simulated for 2.83, 5.77, and 8.02 Gyr respectively, while the rest were run for 9.78 Gyr.

Run Id	**Mass [$M_\odot$]**	**Cooling**	**Trajectory**	**Location of Perturbed Particle for the Shadow Run**
101f	8.40×10^{10}	On	Freefall	centre
100f	8.40×10^{10}	Off	Freefall	centre
111f	8.41×10^{11}	On	Freefall	centre
110f	8.41×10^{11}	Off	Freefall	centre
121f	8.42×10^{12}	On	Freefall	centre
120f	8.42×10^{12}	Off	Freefall	centre
131f	8.45×10^{13}	On	Freefall	centre
130f	8.45×10^{13}	Off	Freefall	centre

Table 2.5: Description of runs where the locations of the perturbed particle are modified. **Note:** In $101p_{center}$ and $101p_{edge}$ perturbed particles were moved closer to the nearest neighbor while in $101p_{HMR}$ it was away from the three closest particles. We also tried moving the particle closer to the nearest neighbor in $101p_{HMR}$ and found no significant difference between the two approaches.

Run Id	**Mass** $[M_\odot]$	**Cooling**	**Trajectory**	**Location of Perturbed Particle for the Shadow Run**	**Displacement of the Perturbed Particle [kpc]**
$100p_{center}$	8.4×10^{10}	Off	Parabolic	Center	0.015
$100p_{HMR}$	8.4×10^{10}	Off	Parabolic	Half Mass Radius	3.60
$100p_{edge}$	8.4×10^{10}	Off	Parabolic	Edge	1.86

Table 2.6: Description of runs where the softening lengths for the lowest mass simulations are modified. Here $\epsilon_{\rm gas}$ and $\epsilon_{\rm DM}$ are softening lengths for gas and dark matter respectively. Subscript numbers in the Run IDs are indicative of scaling relative to the fiducial run which in this case is $101\mathrm{p}_{\epsilon=1}$.

Run Id	**Mass** [$\mathbf{M_\odot}$]	**Cooling**	**Trajectory**	$\epsilon_{\rm gas}$ [**kpc**]	$\epsilon_{\rm DM}$ [**kpc**]	**Location of Perturbed Particle for the Shadow Run**
$100\mathrm{p}_{\epsilon=0.5}$	8.4×10^{10}	Off	Parabolic	0.046	0.232	centre
$100\mathrm{p}_{\epsilon=1}$	8.4×10^{10}	Off	Parabolic	0.093	0.464	centre
$100\mathrm{p}_{\epsilon=2}$	8.4×10^{10}	Off	Parabolic	0.186	0.928	centre
$100\mathrm{p}_{\epsilon=4}$	8.4×10^{10}	Off	Parabolic	0.371	1.857	centre

Chapter 3

Results

In this chapter we review results from the simulation suite detailed in Chapter 2. We re-emphasize that the goal of this work is both to explore the physical differences between the shadow simulations, for runs with modest (freefall) and higher amounts (parabolic) of angular momentum, and to attempt to correlate this with physical variables in the simulation. We are motivated most strongly to look at density since regions of high density undergo more interactions and time-steps and therefore have an increased chance of showing different behaviours. This contrasts to low density regions which often undergo close to ballistic trajectories over a small number of time-steps and which are comparatively straightforward to integrate, at least in theory.

Hence in the context of the above considerations, the primary objective is to look at the correlation of gas density (ρ) with the phase space separation between shadow runs. We define phase-space separation at time t ($\delta(t)$) by extending the Euclidean metric across all

dimensions,

$$\delta(t) = \left[\sum_{i=1}^{N} \frac{(\vec{r}_{i,1} - \vec{r}_{i,2})^2}{R_0} + \sum_{i=1}^{N} \frac{(\vec{v}_{i,1} - \vec{v}_{i,2})^2}{|V_{c,0}|}\right]^{1/2} \tag{3.1}$$

$$= \left[\delta_r^2(t) + \delta_v^2(t)\right]^{1/2} \tag{3.2}$$

where $\vec{r}_{i,1}, \vec{r}_{i,2}, \vec{v}_{i,1}, \vec{v}_{i,2}$ are positions and velocities of particle i in the main run (1) and its shadow run (2), R_0 is the radius of an individual halo at $t = 0$, $V_{c,0}$ is the circular velocity at the edge of the halo at $t = 0$, and N is the total number of gas particles in the simulation since we are only concerned with the gas phase space. The phase space separation δ is a dimensionless quantity with these definitions.

In addition to considering the overall separation we can also look at the distribution of separations between particles in the fiducial versus shadow runs, and how they add with respect to the overall separation. This is a more subtle analysis that connects global behaviours to local differences. Importantly, such an analysis helps us understand whether the differences are related to a small or large number of particles in simulations. Equipartition would tend to argue for these differences averaging out across the simulation, but it is interesting to analyse nonetheless.

We approach the analysis by first reviewing the overall simulation behaviours, and then analyze phase space separations, followed by individual particle behaviour correlations with the density. Lastly, as some issues with momentum conservation were found in the simulations we present a short analysis of the differences in behaviours we found when we corrected for this.

3.1 General Evolution

The key difference that separates cooling and non-cooling runs, in terms of how structure in galaxies form and evolve, is the flow of gas into high density and low temperature states. As gas loses energy through radiative and dynamical processes in cooling runs, it sinks to the bottom of the local or global potential to form a cool core. The density in such a simulated core can far exceed observed (volume-averaged) densities due to the absence of heating that would normally happen in the universe. To alleviate this concern, as discussed earlier, we used a pressure floor which prevents artificial structures from forming below the resolution limit. Such a floor smooths out the cold structure at the centre which is then distributed as a sphere of cold gas. The size and density of the core depends on the amount of mass available to accrete as well the depth of the potential well of the halo.

Another notable difference which changes mass accretion rates on to high density regions is the presence and relative strength of accretion and/or merger-driven shocks. In runs with cooling (e.g. 111p), the initial development of a cool core in turn sees a shock form as early as 200 Myr, see in Figure 3.1. Further evidence of a shock being generated is demonstrated by the steep temperature gradient at radii that increase with time (figure 3.2) as the position at which material hits the accretion shock moves outward. An analytic estimation of the adiabatic sounds speed at 10^6 K gives a value of 70 km s^{-1}, while the edge of the feature moves 10 kpc in 100 Myr, corresponding to a shock speed of around 100 km s^{-1}, so the Mach number is order unity.

There are distinct phases that a merging system undergoes, namely, pre-merger, first

pass, maximum separation, merger, and post-merger. Each of these phases are common to all the runs in our simulations. First pass in parabolic trajectory merger is characterized by periapsis which is the distance at closest approach. In this thesis, we talk extensively about merger completion time, which we characterize through a combination of visual inspection in a visualization software and looking at the behaviour in phase space.

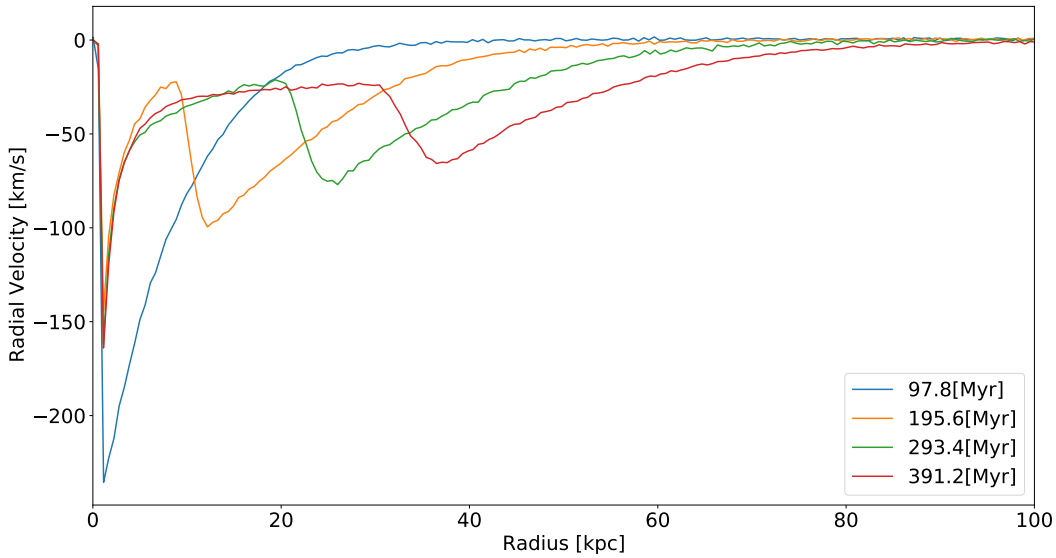

Figure 3.1: Radially-averaged velocity plot for one of the gas systems in 111p, note similar behavior is exhibited in each halo. The centre is assumed to be the centre of mass of the cold core since cold particles sink to the local bottom of the potential. A discontinuity in radial velocity suggests a shock wave, and the increasing radius of the jump with time points to its outward propagation as progressively more material reaches this feature.

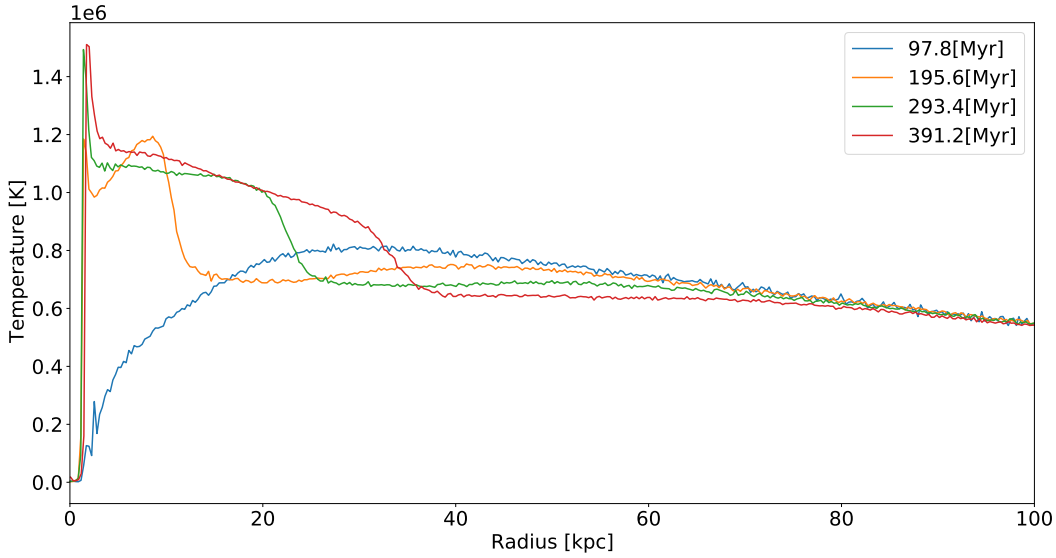

Figure 3.2: Radially binned temperature plot for one of the gas systems in 111p. Similar to Figure 3.1, the temperature discontinuity propagates outward suggestive of material being shock heated.

3.2 Phase Space Evolution

We now analyze how the shadow simulations evolve versus the standard runs in phase space. For completeness, we re-emphasize that the gas evolution is not isolated in the sense that energy can be both given to it and removed via interactions with the dark matter before we consider additional issues like cooling. Because of this issue conservation properties that would normally apply to Hamiltonian systems in phase space e.g. Liouville's Theorem, are not expected to apply here. With phase space being constructed from both position and velocity data we also reemphasize that we have chosen to scale these coordinates by the virial radius and circular velocity at the virial radius, and the definitions of the separations δ_r, and δ_v is given in Equation 3.2.

3.2.1 Parabolic Trajectory

The time evolution of δ_r, δ_v, and δ as shown in Figures 3.3 - 3.5, clearly differentiate galaxy masses in runs with cooling. Lower mass galaxies, with shorter cooling times, exhibit consistently larger separations in phase space. Runs without cooling show very similar behaviour simply because of the way we set up our initial conditions. Each galaxy at different mass scales have all of their properties, including scaled initial velocities, commensurate with the fiducial $8.41 \times 10^{11} M_{\odot}$ galaxy yielding the same interaction times.

All of the runs exhibit a significant increase in phase space separation after periapsis which is at 2.93 Gyr for all runs, with the exception of the lowest mass run with cooling, 101p. 101p has an almost immediate rise in δ_v followed by δ_r showing divergent behaviour quickly. This can likely be attributed to the higher rate of cooling as compared to higher mass galaxies.

The non-cooling runs show a shallowing slope in δ_r once the merger has completed (~ 4.5 [Gyr]), as one would expect: As the merger remnant relaxes, there is a finite limit to δ_r set approximately by the diameter of the remnant. Such a limiting behaviour is also expected on the velocity and this tendency is perhaps stronger in δ_v.

However, cooling introduces more complex behaviours across different masses. No detailed statements could be made regarding 101p due to lack of data beyond periapsis, but the rest of the simulations show a tendency for increasing phase space separation, both in position and velocity, with decreasing mass. However, the way in which a given mass system increases its phase space separation is not clearly predictable by mass. However, to

interpret these results, it is useful to note that 111p and 121p merger remnants have a well defined spiral structure consisting cold gas at the centre. The formation of a flat spiral disk after merger completion is expected from cooling arguments, and the time of formation is dependent on the precise rate of cooling. The lowest mass system, 101p, for example forms rotating disks at the centres of both gas distributions even before the first pass. However, as we will discuss later, 101p has an unusual gain in angular momentum which is a cause for concern regarding robustness of this particular run. Nonetheless, these behaviours taken together clearly seem to show that increased cooling leads to increased possibilities of different behaviours in phase space.

3.2.1.1 Distribution of phase space separations

Figures 3.6 - 3.8 show the distributions of position and velocity phase space separations for individual particles at different times for 120p and 121p simulations. The distributions of separations between particles in the fiducial versus shadow run are always sorted from smallest to largest, so there is no correspondence along the x-axis to given particle, it is descriptive of the global behaviour of the distribution.

Figure 3.6 and 3.7 show the distributions for the non-cooling 120p pair. The stand out feature is the equilibrium after merger completion, more so in the velocity space than in position space. However, position separations continue to grow ever so slightly while velocity separations have roughly reached the peak suggesting that even the slightest variations in velocities produce a non-insignificant change in positions. Early evolution is slow; By 200 Myr, only $\sim$25% of the particles have gained some separation in position phase space as

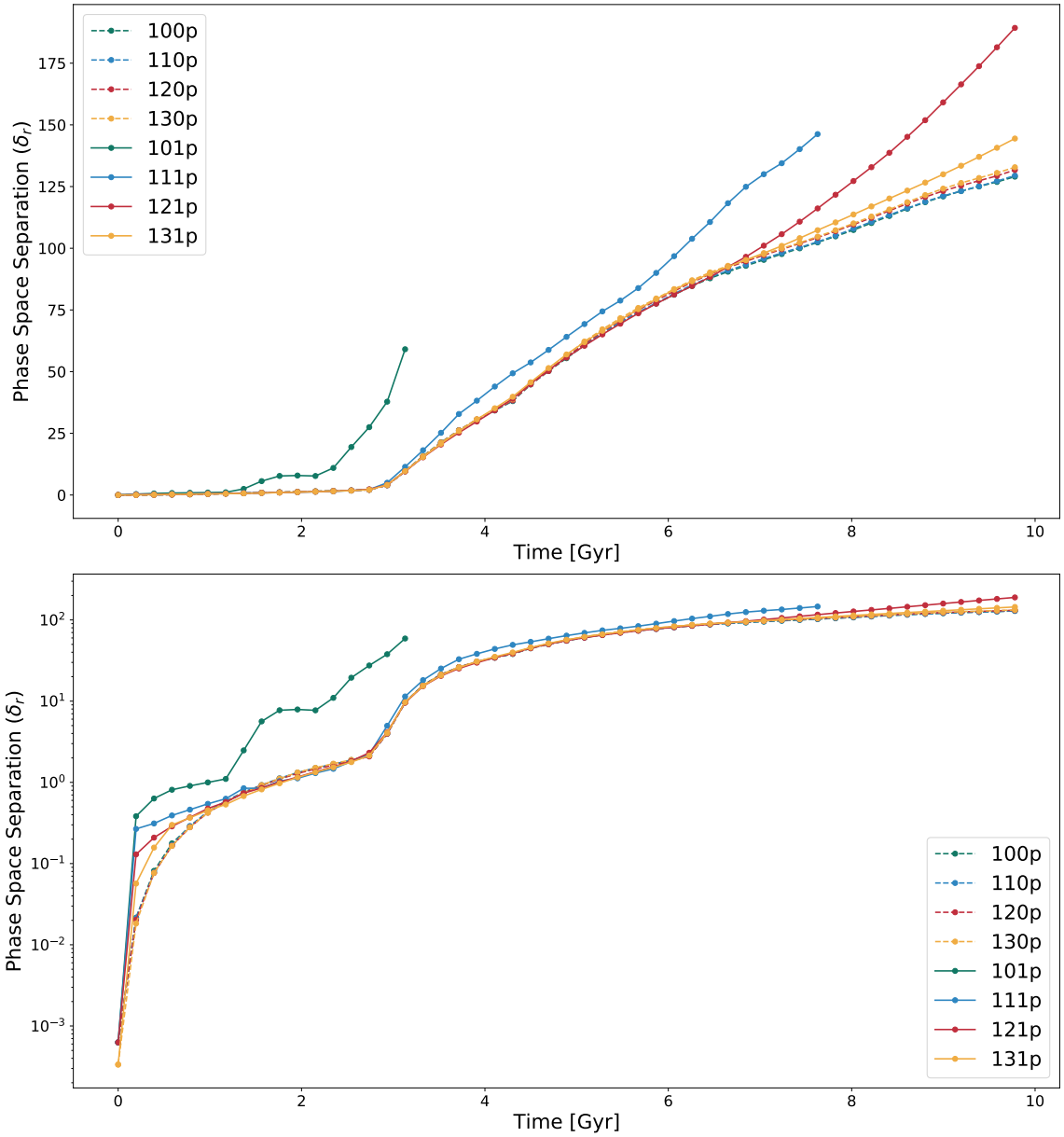

Figure 3.3: Parabolic Trajectory: Time evolution of the position phase space separation (δ_r) between shadow runs. Solid lines indicate cooling-on runs and dashed cooling-off. Top panel is linear and bottom log scaled to better visualize early and late term evolution. There is a trend with mass in the absolute value of the phase space separation but the slopes differ at later times suggestive of the impact of pre-merger differences.

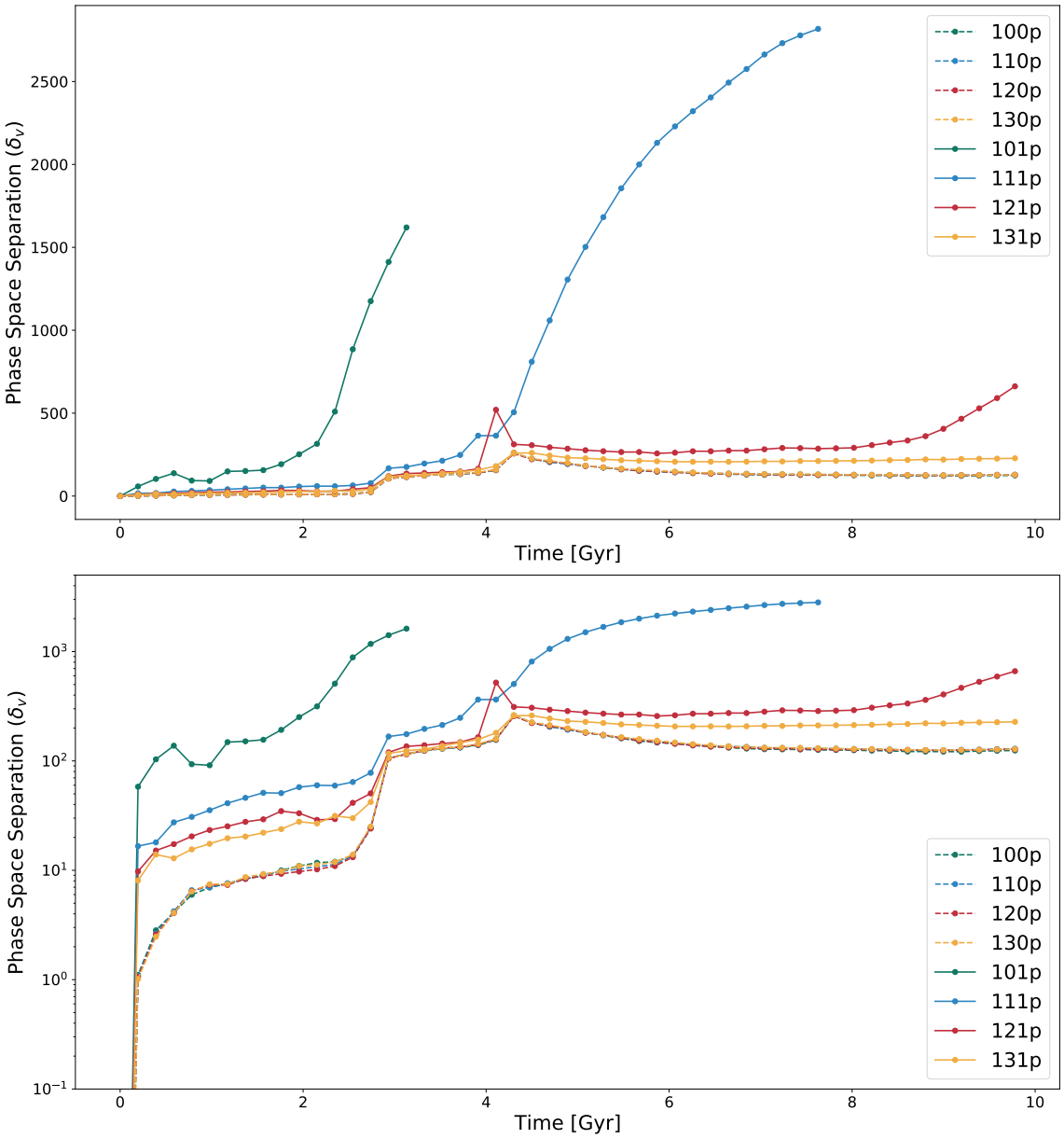

Figure 3.4: Parabolic Trajectory: Time evolution of the velocity phase space separation (δ_v) between shadow runs. Solid lines indicate cooling-on runs and dashed cooling-off. Top panel is linear and bottom log scaled. Behavior is similar to δ_r but early epochs have larger variations with mass. There is a multiplicity of slopes post-merger here as well.

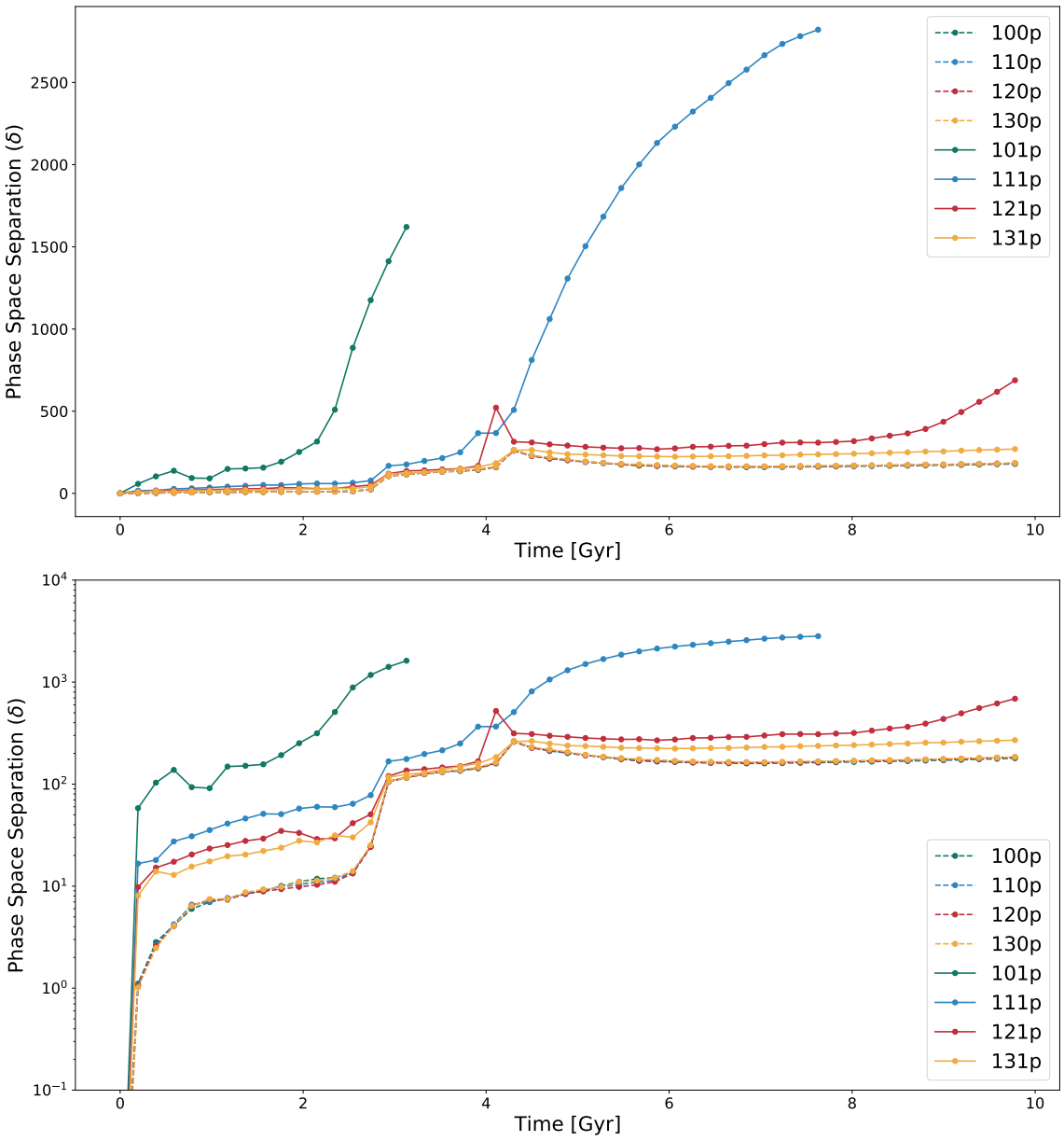

Figure 3.5: Parabolic Trajectory: Time evolution of the total phase space separation (δ) between shadow runs. Solid lines indicate cooling-on runs and dashed cooling-off. Top panel is linear and bottom log scaled. Here δ_v is dominant making δ and δ_v visually similar.

compared to ∼70% in the velocity space.

In the corresponding cooling-on pair (Figures 3.9 and 3.8), early on, velocity differences grow somewhat more quickly than position. At 200 Myr, nearly 70% of the particles have not experienced any changes in position phase space and out of the 30% that have, a large fraction is coming from a small number of particles from the high density regions with shorter cooling times. On the other hand most particles have gained some separation in the velocity space, but the contribution from a small number of particles is still significant compared to the rest. Later evolution (post merger) appears to be slowing down in both position and velocity spaces. Although the system has cooling and hence does not approach an equilibrium in any true sense, the large-scale evolution is largely ended after the merger and so an appearance of distributions becoming more similar is not unexpected.

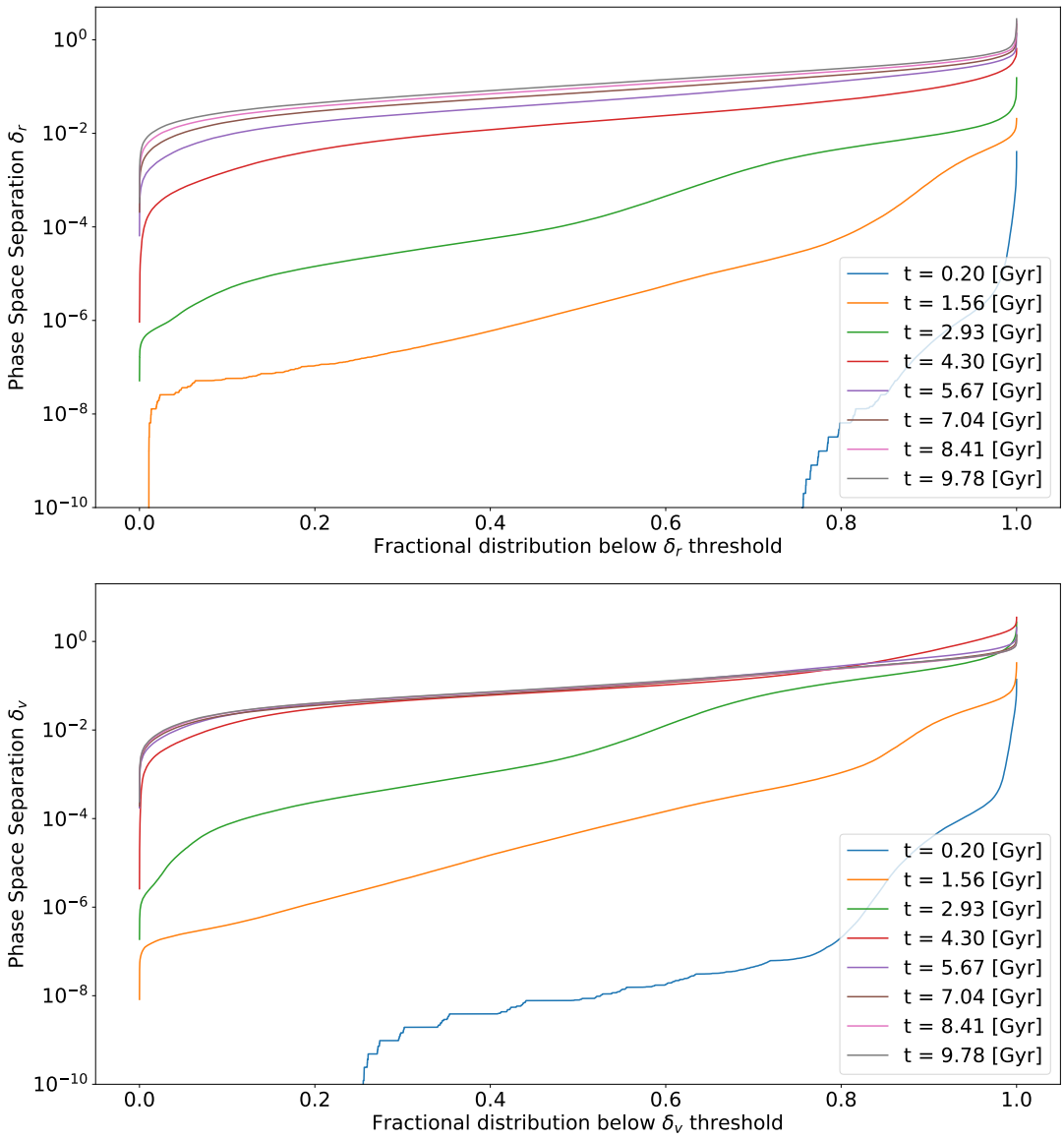

Figure 3.6: Parabolic Trajectory: Distributions of phase space separations by individual components, position (δ_r, top panel) and velocity (δ_v, bottom panel) at different times for 120p. Notice the equilibrium after merger completion and similar scales for both components. Velocity separations reach equilibrium much earlier than positions.

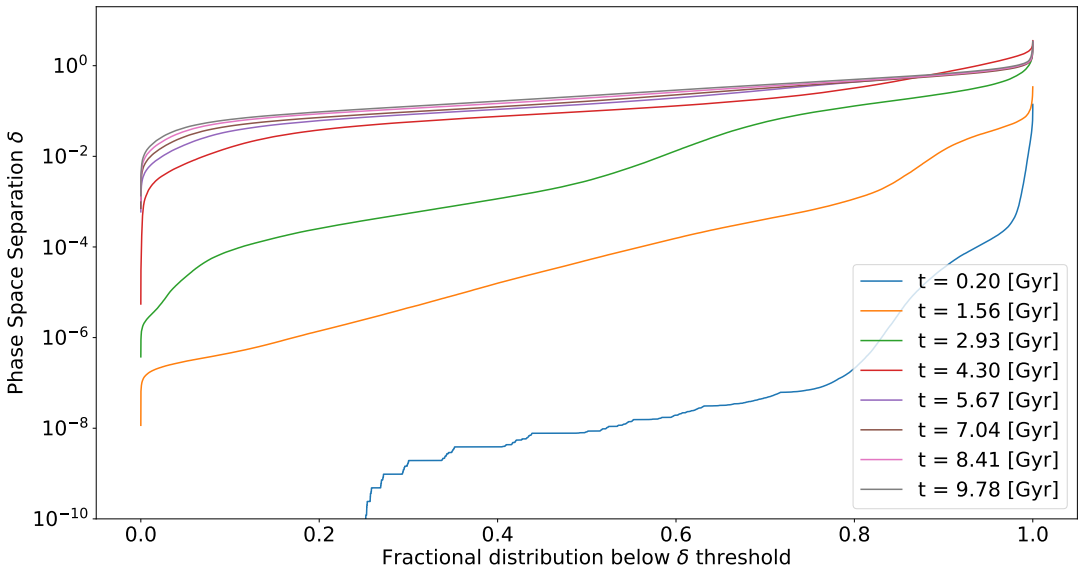

Figure 3.7: Parabolic Trajectory: Total phase space separation (δ) distributions for 120p at different times. Notice the lopsided evolution where the higher end of the distribution accumulates changes faster than the lower end.

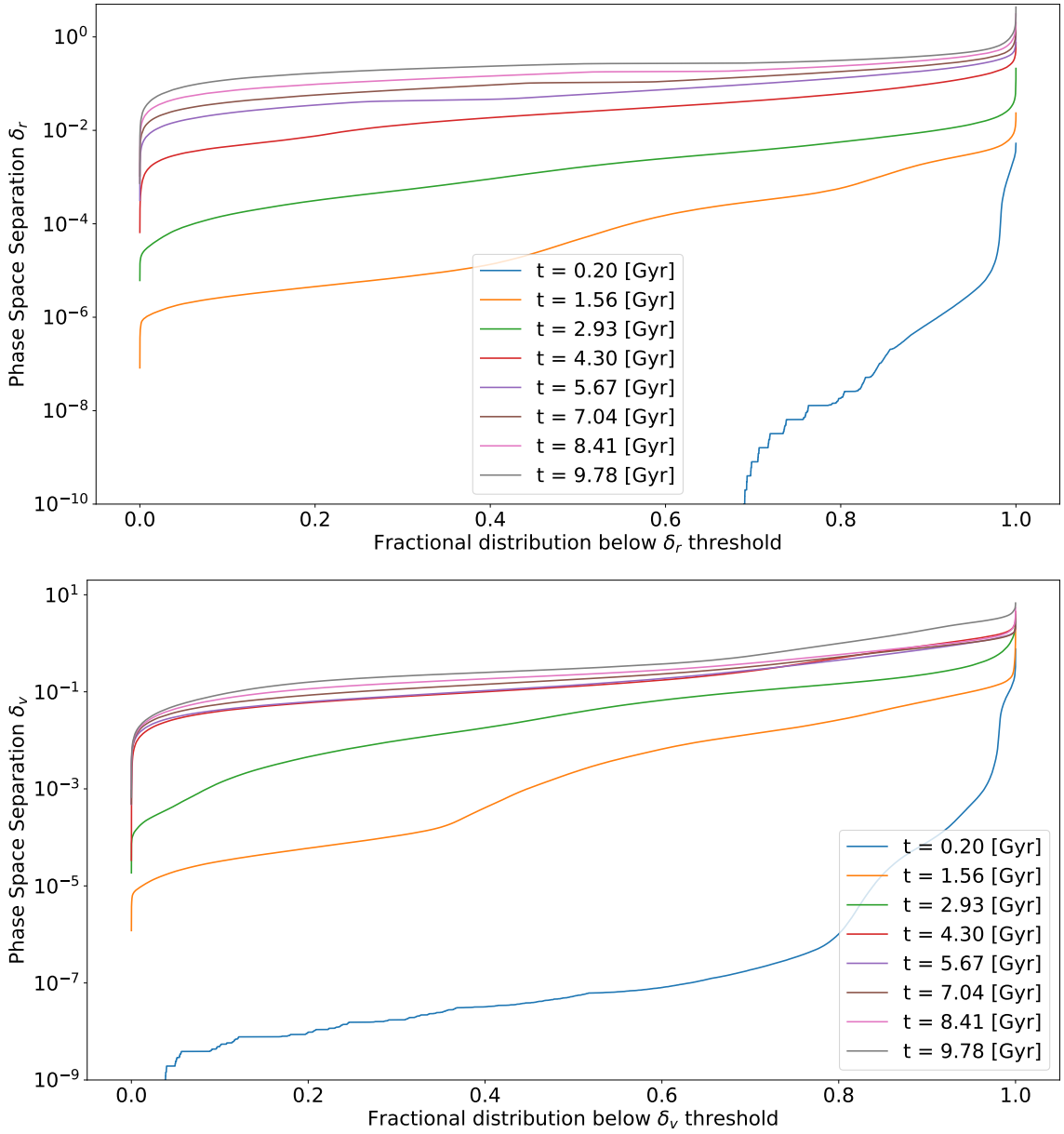

Figure 3.8: Parabolic Trajectory: Distributions of phase space separations by individual components, position (δ_r, top panel) and velocity (δ_v, bottom panel) at different times for 121p. Although beginning with a much larger discrepancy between regions, the final positional differences are much more evenly distributed.

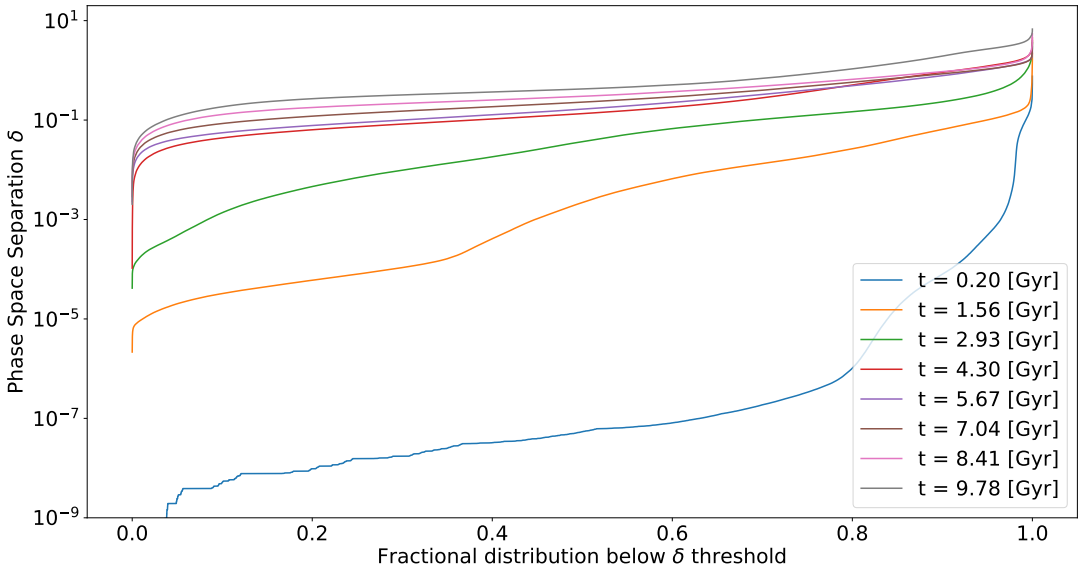

Figure 3.9: Parabolic Trajectory: Total phase space separation (δ) distributions for 121p at different times. When compared to the cooling-off counterpart (figure 3.7) we can notice right away the order of magnitude difference at later times and even more pre-merger, indicative of the variations introduced by cooling.

3.2.2 Freefall Trajectory

The key difference between the parabolic trajectory versus the freefall trajectory is the reduced amount of angular momentum in the collision. From a numerical integration perspective this arguably puts more emphasis on the gravitational and hydrodynamic solvers as the final mass distribution will be more condensed with fewer outlying trajectories that are largely ballistic in nature. Because this collision begins with zero initial velocity, as opposed to the parabolic trajectory which by kinematic necessity includes an initial boost, most of the merger evolution occurs after 6 Gyr.

The time evolution of δ_r, δ_v, and δ for the freefall suite can be seen in Figures 3.10 - 3.12. There is again a clear trend in the magnitude of phase space separation with galaxy mass. Due to time constraints, we have limited data for 101f (2.84 Gyr), 111f (5.77 Gyr) and 121f (8.02 Gyr). Nonetheless, we can notice similarities in the overall evolution between freefall and parabolic runs. There are differences in the scales of velocity separations between them with parabolic suite expectedly exhibiting consistently larger separations in the lower mass mergers. Combining this with the fact that these low mass runs diverge significantly from other simulations at similar time scales in both freefall and parabolic runs regardless of their initial angular momentum differences, suggests that cooling is the primary source of differences in the early evolutionary stages. Another notable behavior is the reduction in δ_v post merger (after $\sim$ 7 [Gyr]) in freefall non-cooling runs in contrast to its parabolic counterparts where it simply flattens.

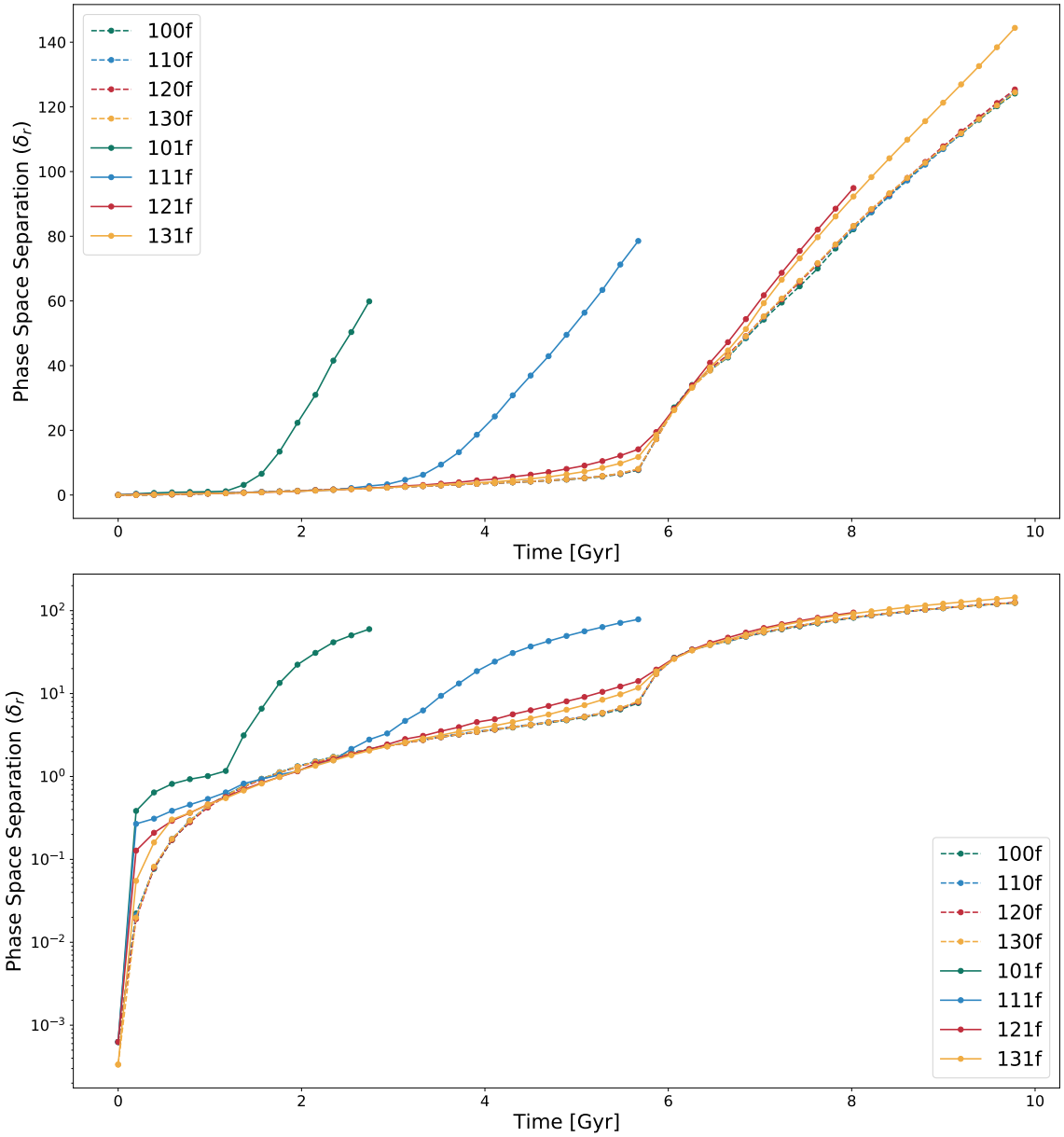

Figure 3.10: Freefall Trajectory: Time evolution of the position phase space separation (δ_r) between shadow runs. Solid lines indicate cooling-on runs and dashed cooling-off. Top panel is linear and bottom log scaled to better visualize early and late term evolution. Notice how the divergence in 101f and 111f occurs much earlier than other cooling and non-cooling runs despite going through similar merger dynamics.

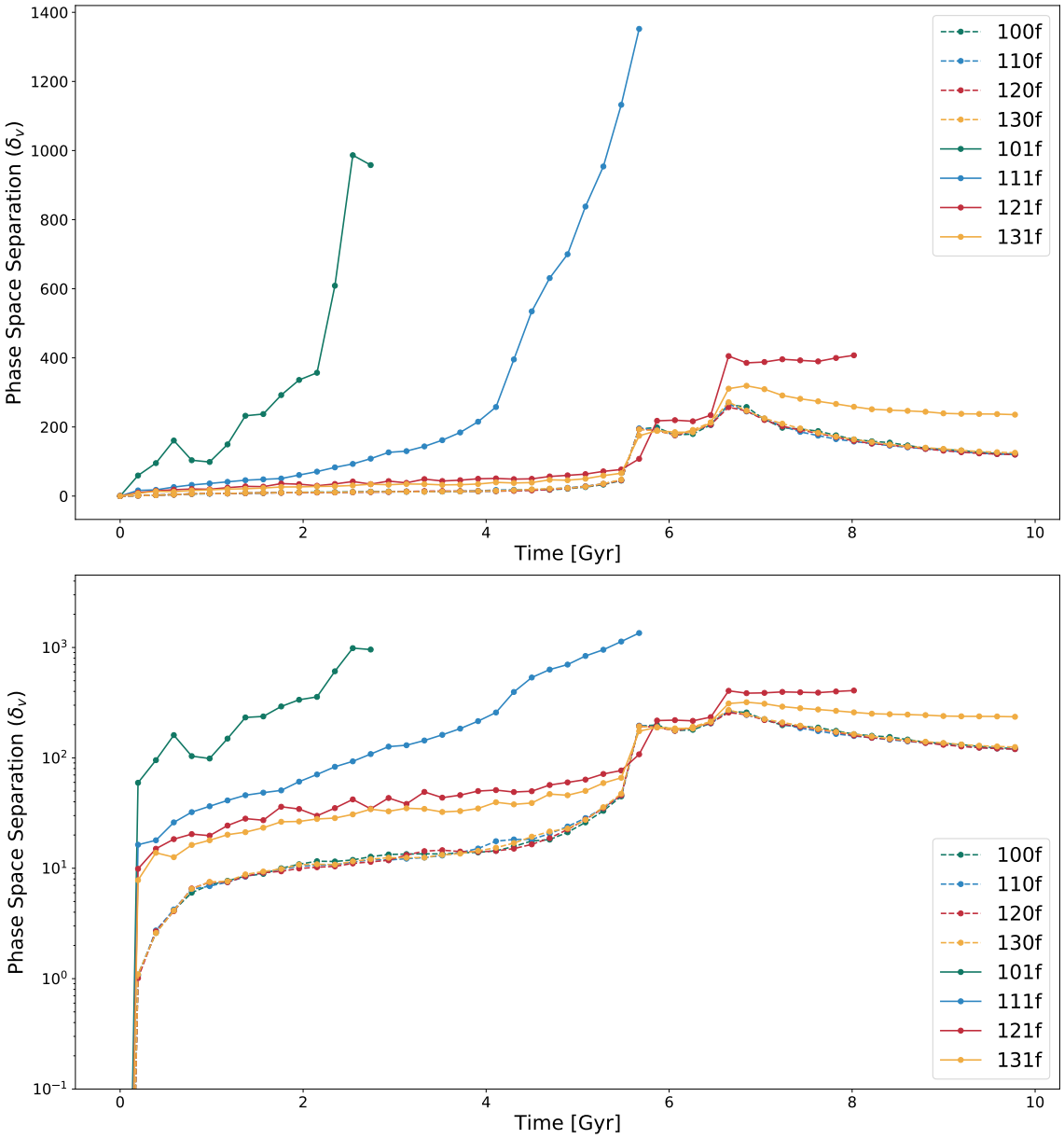

Figure 3.11: Freefall Trajectory: Time evolution of the position phase space separation (δ_v) between shadow runs. Solid lines indicate cooling-on runs and dashed cooling-off. Top panel is linear and bottom log scaled. Distinct merger phases are visible from 5.5 to 7 Gyr, that are not apparent in δ_r (figure 3.10).

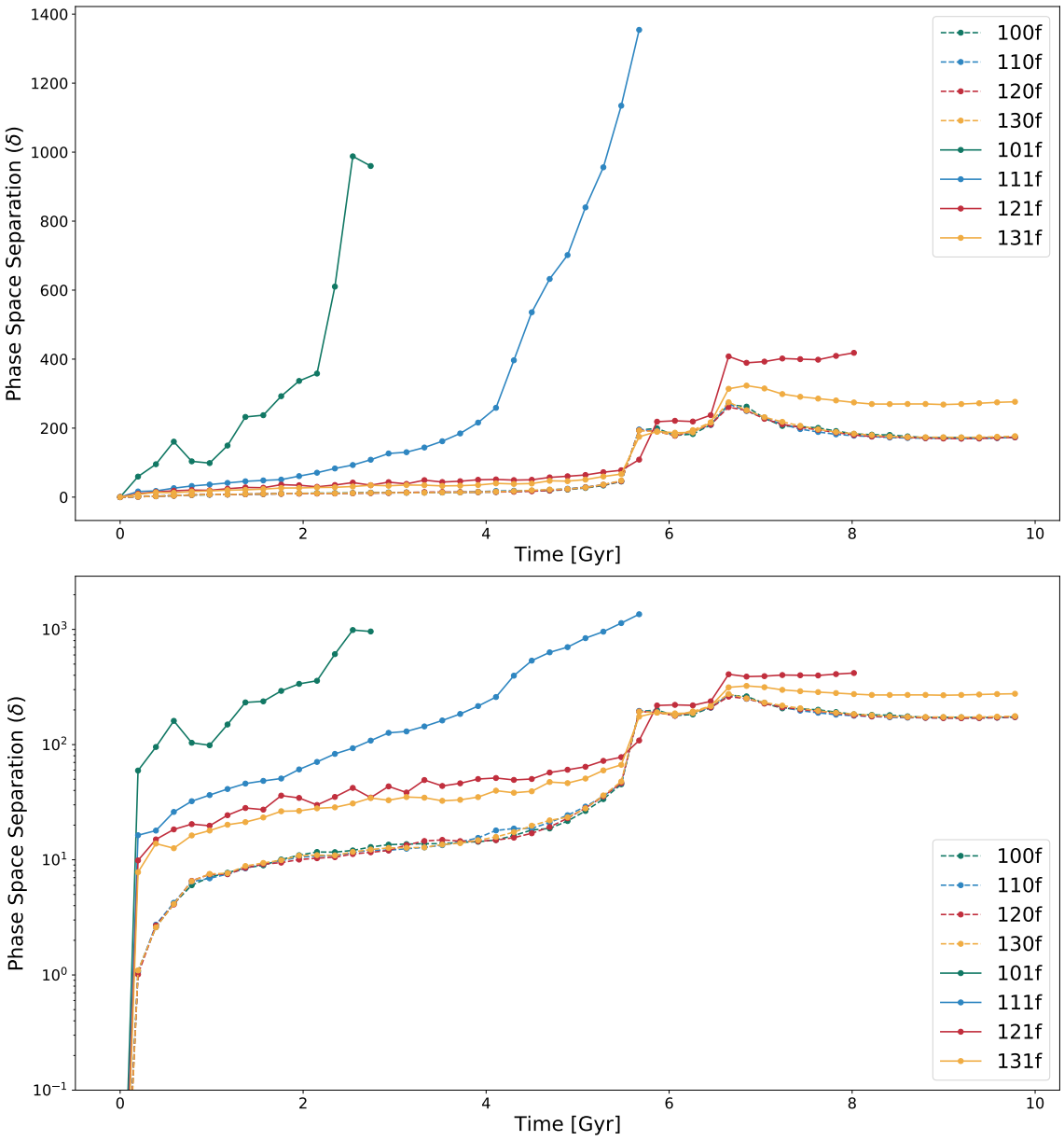

Figure 3.12: Freefall Trajectory: Time evolution of the total phase space separation (δ) between shadow runs. Solid lines indicate cooling-on runs and dashed cooling-off. Top panel is linear and bottom log scaled.

3.2.2.1 Distribution of phase space separations

Phase space separation distributions for freefall runs 120f and 121f at various times are shown in Figures 3.13 - 3.15. While nothing stands out particularly for the non-cooling pair as compared to its parabolic counterpart, cooling-on pair has a more interesting behavior. Total separation δ looks similar to the parabolic run 121p where small number of particles contribute the most in the beginning. δ_r and δ_v both have similarly shaped distributions at similar scales. It seems to have a more progressive evolution across the distribution as opposed to 121p which has a slightly skewed evolution, towards larger values in δ_v and smaller values in δ_r post merger. This kind of inconsistent evolution where we see smaller position and larger velocity separations aligns with the fact that there is a flat disk present in the parabolic pair post merger which is not found in the freefall pair.

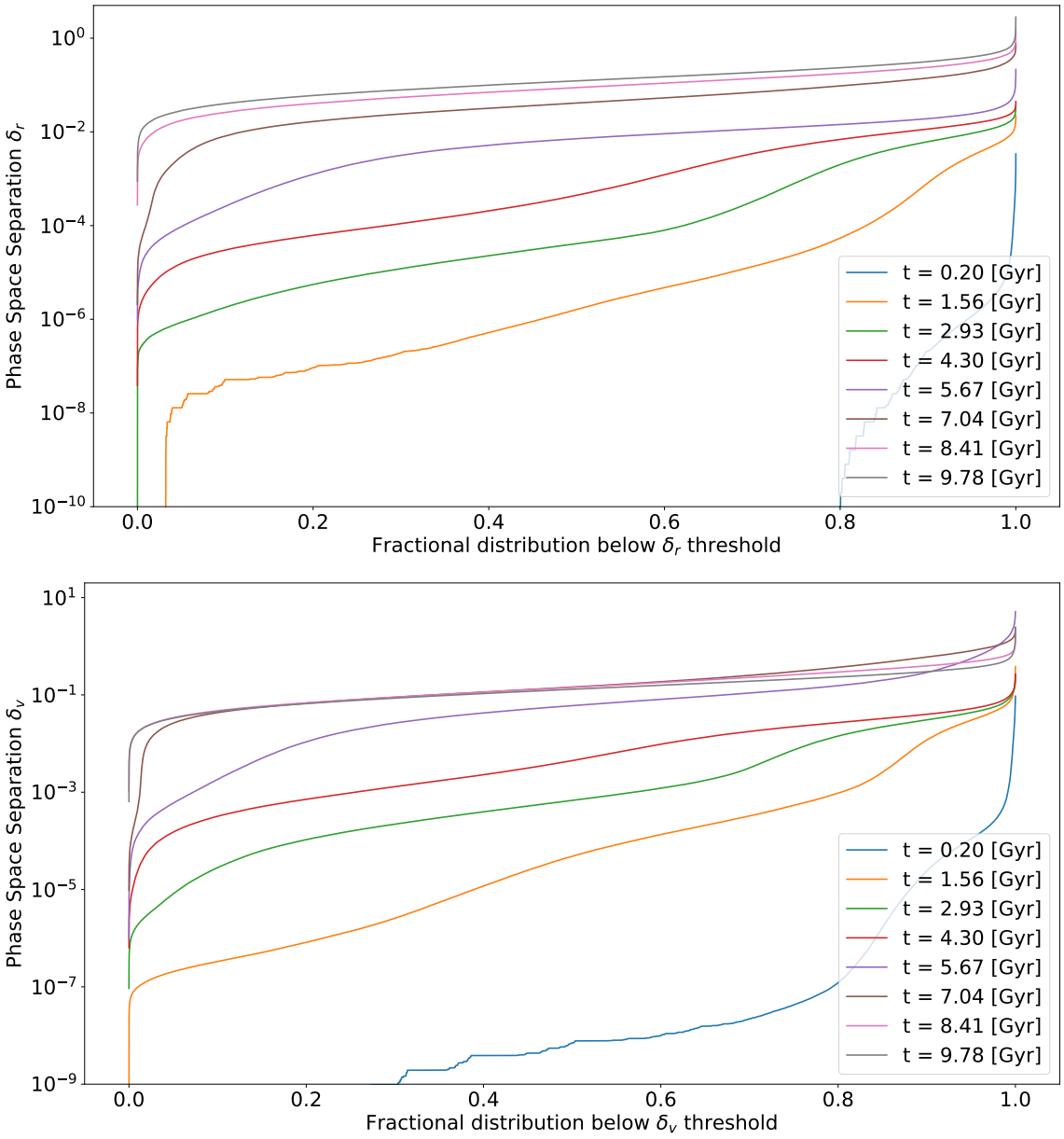

Figure 3.13: Freefall Trajectory: Distributions of phase space separations by individual components, position (δ_r, top panel) and velocity (δ_v, bottom panel) at different times for 120f.

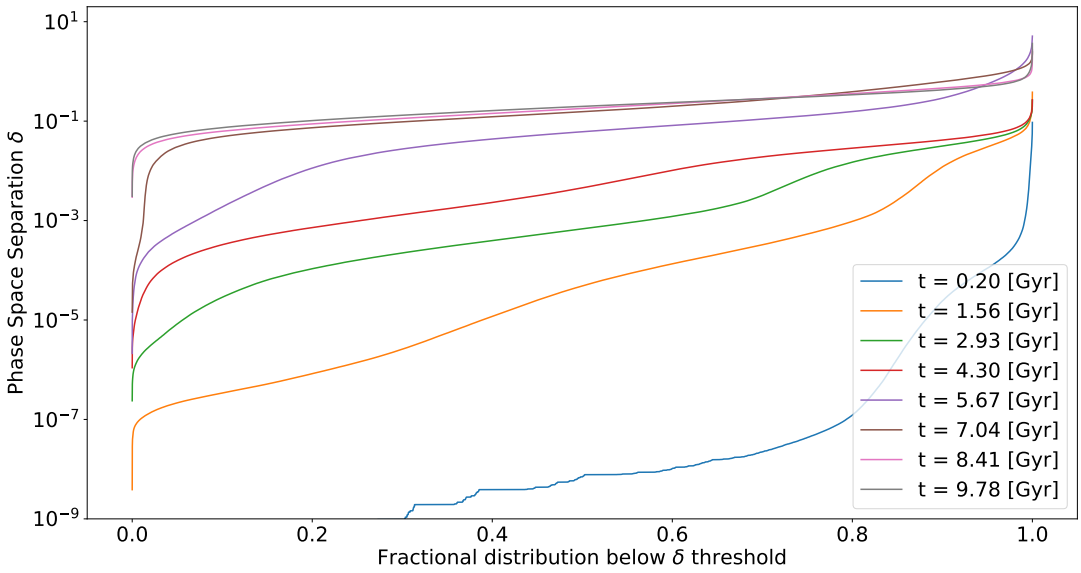

Figure 3.14: Freefall Trajectory: Total phase space separation (δ) distributions for 120f at different times. As compared to the same plot for the parabolic run (figure 3.7), evolution here is less lopsided, likely because of the longer merger time-scales.

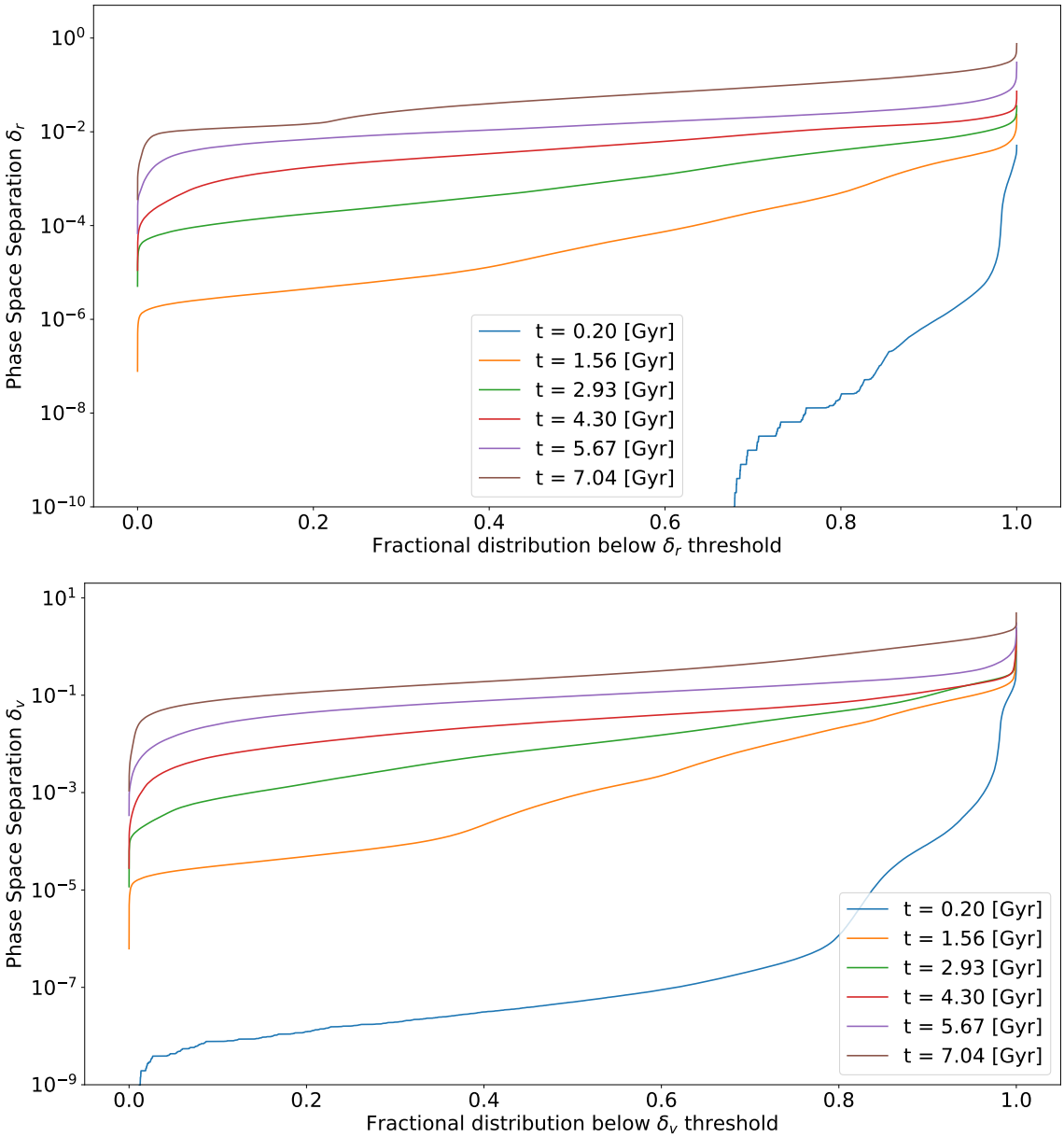

Figure 3.15: Freefall Trajectory: Distributions of phase space separations by individual components, position (δ_r, top panel) and velocity (δ_v, bottom panel) at different times for 121f.

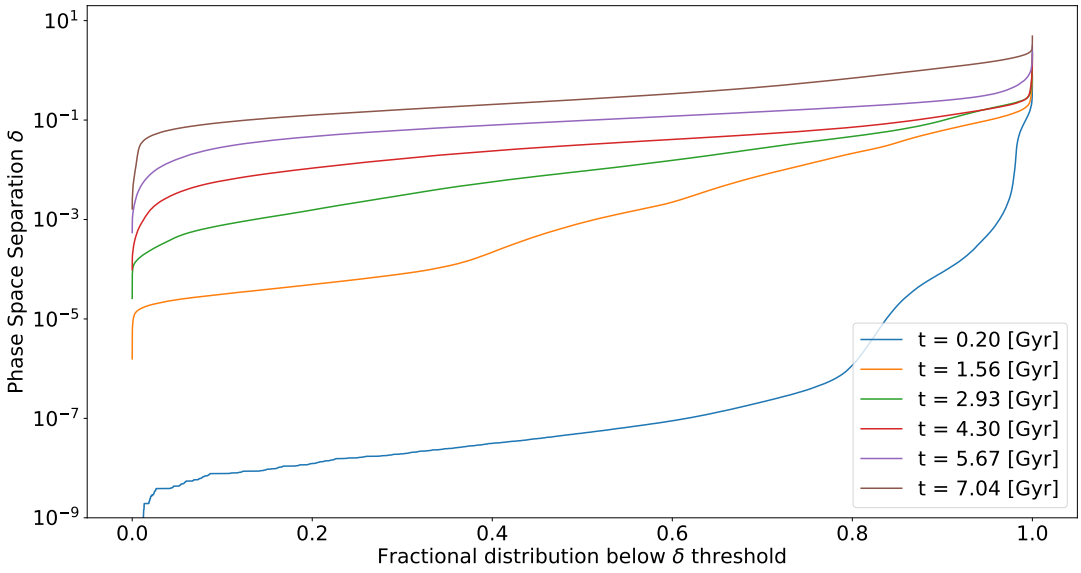

Figure 3.16: Freefall Trajectory: Total phase space separation (δ) distributions for 121f at different times. Similar to the parabolic counterpart (figure 3.9), a small fraction of particles, presumably cold, get separated in phase space right from the onset and do not undergo evolution much further.

3.3 Lyapunov Exponents

We now quantify the phase space evolution using Lyapunov exponent (see eq. 1.1) formalism and inferred doubling time[1]. We emphasize that a full Lyapunov analysis would require an entire spectrum of phase space differences, making our exploratory data a starting point for future investigations. In Section 3.2 we observed that the phase space separations go through an evolution and thus only looking at the overall run-time value, we would fail to capture the nuances of distinct merger phases. Thus we have used two time-scales to calculate the aforementioned quantities, namely the entire simulation (table 3.1) and post-merger phase (table 3.2). An exponential of the form (ae^{bx}) was fit at these time-scales using the least-squares method with minimization performed by a trust region reflective algorithm implemented in Scipy (Virtanen et al. 2020). Looking at the phase space evolution plots, it is visually clear that almost no simulation has an exponential form throughout the entire run-time, and thus fitting it with a single exponential function is not accurate and only representative of a rough estimate.

As shown in the Tables 3.1 and 3.2, post-merger Lyapunov exponents are significantly smaller than the overall ones, suggestive of slowing of the characteristic growth of run separations. Since our initial conditions were scaled in mass and the phase space separations were all consistent, we see virtually no difference in non-cooling runs. Note, because our data for some low mass simulations is incomplete, two of them being pre-merger only, we cannot give precise quantitative analyses for all epochs. Qualitatively, we see shorter doubling times

[1]Doubling time is the amount of time it takes for a given quantity to double in size or value at a constant growth rate.

with faster cooling.

Table 3.1: Lyapunov exponents (λ) and doubling times (t_D) for entire simulations. **Note:** 101p and 111p were only run for 3.13 and 7.73 Gyr respectively while the rest for 9.78 Gyr.

Mass $[M_\odot]$	**Cooling On Parabolic**		**Cooling Off Parabolic**		**Cooling On Freefall**		**Cooling Off Freefall**	
	λ $[Gyr^{-1}]$	t_D [Gyr]	λ $[Gyr^{-1}]$	t_D [Gyr]	λ $[Gyr^{-1}]$	t_D [Gyr]	λ $[Gyr^{-1}]$	t_D [Gyr]
8.40×10^{10}	1.38	0.50	0.13	5.17	1.25	0.55	0.23	2.94
8.41×10^{11}	0.43	1.58	0.13	5.10	0.90	0.77	0.23	2.96
8.42×10^{12}	0.22	3.14	0.13	5.08	0.49	1.41	0.23	2.94
8.45×10^{13}	0.15	4.46	0.13	5.11	0.25	2.76	0.23	2.95

Table 3.2: Lyapunov exponents (λ) and doubling time (t_D) for all runs post merger. Merger completion times used are 3.91 Gyr (parabolic) and 6.36 Gyr (freefall). **Note:** 101f, 111f, and 121f were only run for 2.83, 5.57, and 8.02 Gyr respectively while the rest for 9.78 Gyr.

Mass $[M_\odot]$	**Cooling On Parabolic**		**Cooling Off Parabolic**		**Cooling On Freefall**		**Cooling Off Freefall**	
	λ $[Gyr^{-1}]$	t_D [Gyr]	λ $[Gyr^{-1}]$	t_D [Gyr]	λ $[Gyr^{-1}]$	t_D [Gyr]	λ $[Gyr^{-1}]$	t_D [Gyr]
8.40×10^{10}	n/a	n/a	0.05	13.26	n/a	n/a	0.03	23.02
8.41×10^{11}	0.39	1.74	0.05	13.16	n/a	n/a	0.03	24.30
8.42×10^{12}	0.18	3.75	0.05	12.81	0.19	3.49	0.03	26.06
8.45×10^{13}	0.09	7.66	0.05	13.13	0.05	13.45	0.02	28.71

3.4 Density-Phase Space Correlation

We now turn to analyzing whether differences in particle orbit trajectories and velocities, equivalently the phase space "particle subspace" differences, can be correlated to other physical variables. If there is a strong correlation it means that we can predict what the potentially less reliable parts of a simulation are.

For the local density of each particle we use the density field from GIZMO snapshot files and focus our analysis on densities of the fiducial run. With both a fiducial and shadow run the corresponding particles in one simulation versus another may have different densities. However, as long as we are consistent in choosing one particular simulation and do not expect biases for the shadow versus fiducial run, this should be a statistically reasonable approach.

The correlation between the density and phase space separation (position or velocity or total) was calculated using the Spearman rank correlation coefficient which is defined as,

$$\psi = 1 - \frac{6 \sum_{i=1}^{N} d_i^2}{N(N^2 - 1)} \tag{3.3}$$

The method works by assigning each particle i a rank in density and phase space separation independently with respect to other particles. Once they are ranked, we only need the difference between ranks for each particle i to get the correlation coefficient ψ. For example, if particle i is ranked 2 in density and 5 in phase space separation, its corresponding d_i is $5 - 2 = 3$. The value of ψ ranges from -1 to $+1$, with -1 signifying a perfect anti-

correlation and +1 a perfect correlation. Spearman rank correlation was used instead of Pearson rank correlation, since the latter assumes the underlying variables to be normally distributed which cannot be assumed to be true in this case as the density and phase space distributions show skewed behaviours.

As briefly mentioned earlier (section 1.4) while motivating this study, if we expect cooling to be responsible for inflating small scale variations, we should see a high correlation between density and δ since cooling is directly dependent on density.

3.4.1 Parabolic Trajectory

The correlations for the parabolic trajectory suite of simulations are shown in Figures 3.17, 3.18, and 3.19. Clearly, as expected, all of the runs without cooling behave nearly identical throughout the merger and subsequent virialization. This is expected since every galaxy has all of its physical properties commensurate with a fiducial one which in our study is the $8.42 \times 10^{11} M_{\odot}$ galaxy and without any additional physics to vary the mass dependence of their evolution, they behave identically.

On the other hand, in the presence of cooling, the behaviour varies significantly with galaxy mass. For a given mass, the correlation in cooling-on runs is stronger at the beginning of the simulation than their cooling-off counterparts, the behaviour persists for approximately the first Gyr. This is likely due to the fact that with cooling on, gas loses thermal "support" instantaneously and dense cooled cores begin forming at the centres of respective halos. The integration challenges of denser regions seed growth in differences which makes calculated physical properties in these regions less precise. Over time, these

differences push denser regions farther apart in phase space with respect to fiducial versus shadow runs.

A particular behaviour that stands out is that the velocity component differences are dominant in the correlations with overall δ. The smooth increase in δ_r correlations with density differs greatly from the sharp increase in δ_v correlations. The timescale of response of higher density regions to perturbations is naturally faster than lower densities and the velocities of particles there can be expected to become separated from their shadow runs. Positional differences are expected to lag behind velocity differences simply because changes in position are contingent upon that of velocity. Note this is not necessarily a one-way exchange it is possible that positional differences could turn into velocity differences at later stages of evolution (e.g. consider a pair of librating pendulums on slightly different frequencies, they may eventually reach the same displacement at some point but with different velocities).

The next noticeable feature is the small dip after the initial rise at around 2 Gyr and the subsequent growth in correlation out to 2.93 Gyr. As the merger progresses, the first regions to be affected by dynamics are the outerlying parts of the halos in contact along the line of the collision. As discussed above, low density regions contribute less to the phase space separation initially, however, at the early stages of the merger, the collision boundaries of both halos experience an increase in pressure following compression from higher density regions "beneath" them coming together. The pressure build up and rise in temperature set off minor perturbations in these low density regions which result in a dip in the correlation, in essence variations start accumulating in the lowest density parts of the simulation.

However, over time, the density in these regions increases substantially, in turn changing the overall correlation to be less impacted by these previously lower density regions. The low mass galaxies where cooling is significant, do not have correlation as strong as their cooling-off parallels again, likely because of other dominant processes like shocks from the central cores.

All of the runs exhibit a decline in correlations after periapsis (2.93 Gyr for all runs) except 101p which declines much earlier. This decline is especially steep for cooling-on runs and shallower for those without. As the galaxies approach periapsis, gas particles gain velocity. This dynamical interplay allows some loosely bound gas particles to gain large amounts of momentum and are thus dispersed outwards, and these high velocities naturally produce potentially large differences between particles in phase space. These particles make their way through the low density regions. The net impact is thus: Parts of the simulation show large differences at low density, which in turn appears to bring the strength of the correlation down after the periapsis. This process is called a merger shock, and although it is weak in our simulations, especially at higher masses, it causes significant amount of material to be transported from the high to low density regions.

The second lowest mass cooling-on pair (111p) anti-correlates in position space (figure 3.18) at later times. Since we were not able to run 101p for more than 2.93 Gyr, we cannot definitively claim the anti-correlation, however, based on the trend with galaxy mass, we can extrapolate that might well be the behaviour shown. These runs have the most cooling and consequently more mass in and around the cooled cores to disperse after the periapsis. Given the fact that these particles have already gained a significant variation before traversing out

to the low density regions, the original perturbations in velocities can cause them to be in vastly different positions. On the other hand, central cores have a rather limited position space freedom, since insufficient heating and self gravity prevents the cores from getting physically bigger. It is important to note that this phenomenon is likely only visible in our simplistic simulations. With the addition of feedback behaviours would undoubtedly be made more complex by cycling between high and low density regions due to energetic feedback.

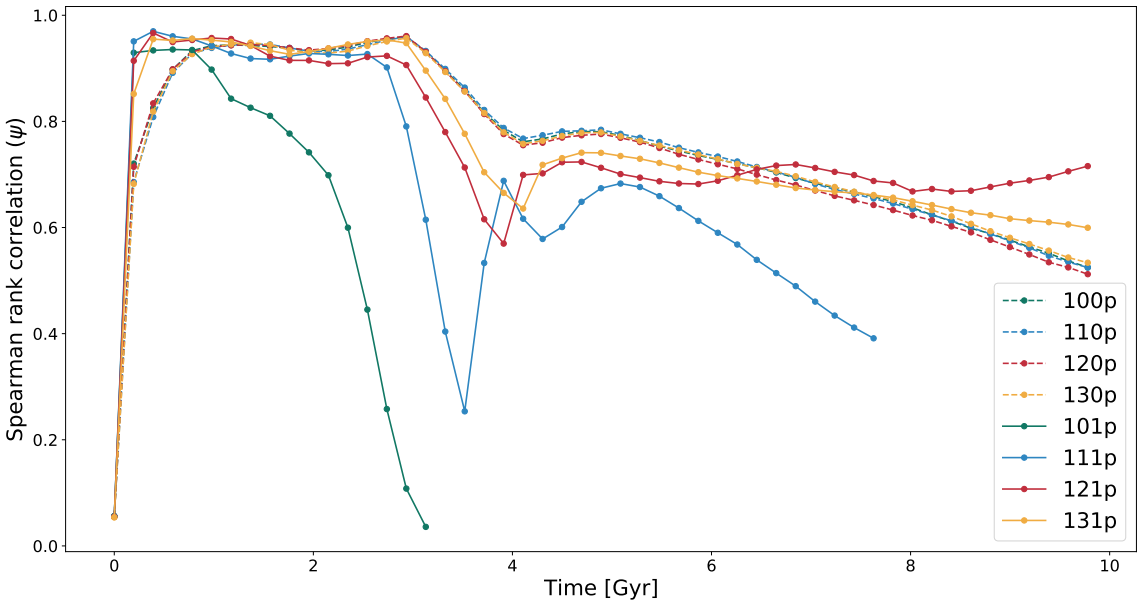

Figure 3.17: Parabolic Trajectory: Spearman rank correlation coefficient for gas density and total phase space separation (δ) between shadow runs. Solid lines indicate cooling-on runs and dashed cooling-off. Notice the unusual behavior of 121p at later times. There is a clear trend in loss of correlation with cooling rate.

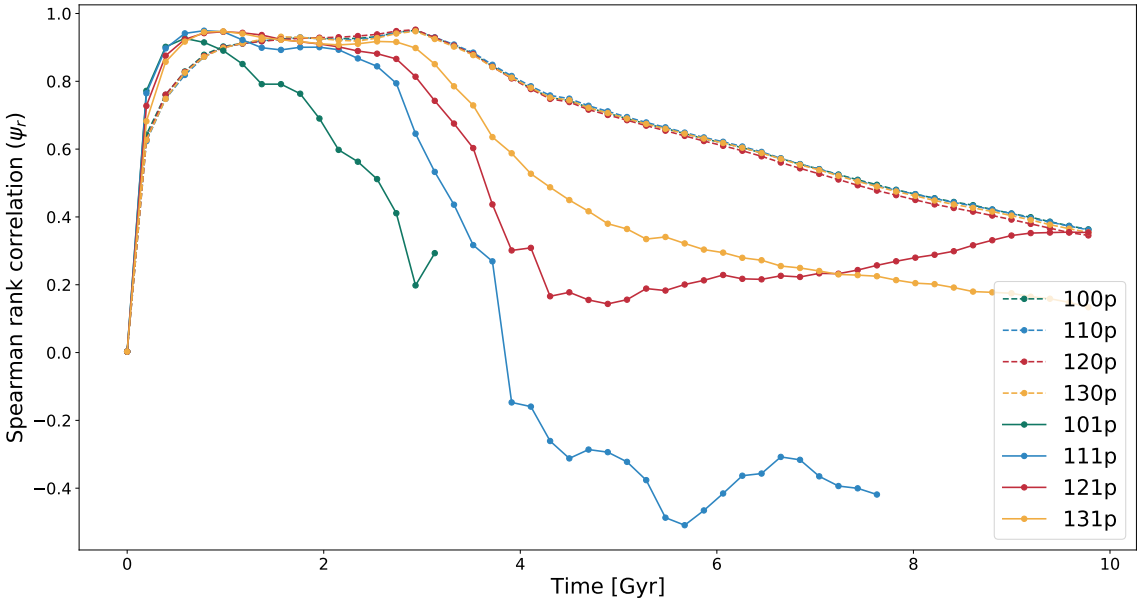

Figure 3.18: Parabolic Trajectory: Spearman rank correlation coefficient for gas density and position phase space separation (δ_r) between shadow runs. Solid lines indicate cooling-on runs and dashed cooling-off.

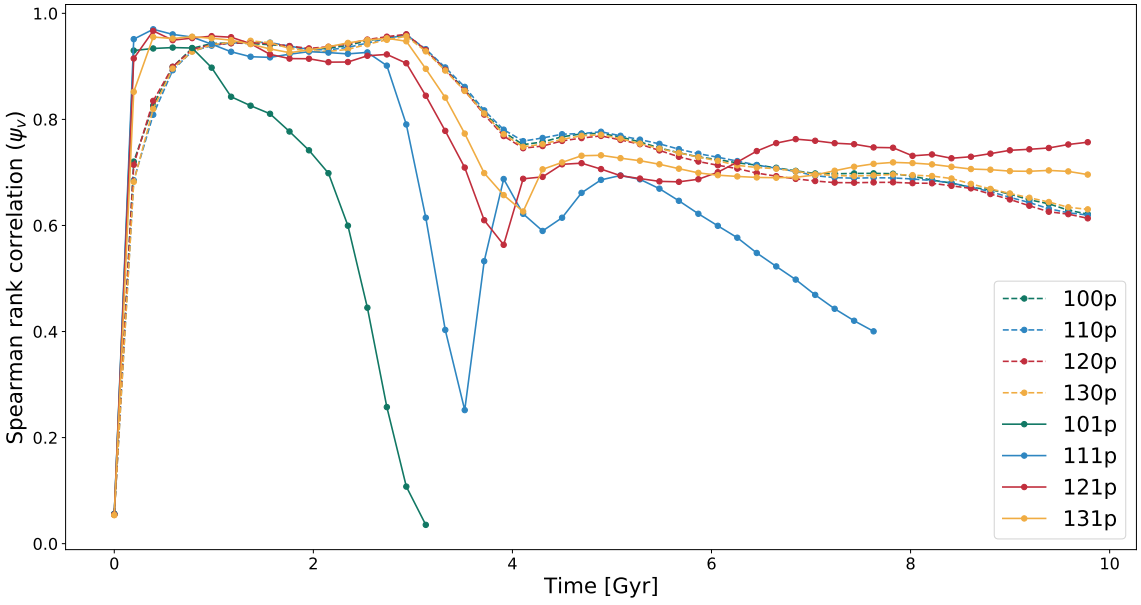

Figure 3.19: Parabolic Trajectory: Spearman rank correlation coefficient for gas density and velocity phase space separation (δ_v) between shadow runs. Solid lines indicate cooling-on runs and dashed cooling-off.

3.4.2 Freefall Trajectory

The correlation between density and phase space separation for a freefall merger largely follows a similar trend as the parabolic trajectory scenario. Non-cooling runs have identical evolution while cooling on simulations have a significant scatter. In the freefall scenario, galaxies initially start at rest relative to each other, which makes the merger timescales longer than the parabolic ones. For example, merger completion occurs at $\sim$ 4.5 Gyr in parabolic runs as opposed to $\sim$ 7 Gyr in the freefall runs. Longer earlier epochs give more gas the opportunity to cool before the merger occurs. We can notice right away (figure 3.20) that the loss in correlation is dependent on cooling time.

101f and 111f which have shorter cooling times, also appear to have accretion shocks forming at $\sim$ 1 Gyr (figure 3.1 for reference). Supersonic gas falling towards the centre encounters in-falling gas with subsonic velocities or gas at rest which in turn slows it down forming an accretion shock. These shocks are not as strong in 121f and non-existent in 131f. The outward propagation of such a shock is a major factor in seeding phase space separations in increasingly lower densities bringing down the correlation earlier than galaxies with less cooling. Note that these shocks are also present in the parabolic runs, but since the merger timescales are shorter, they become less important. 101p was the only run with incredibly strong cooling which brought down the correlation much earlier than the higher mass runs.

Lastly, in contrast to the parabolic runs, even the higher mass cooling-on runs exhibit an anti-correlation (or at least begin to) in position space (figure 3.21) post merger.

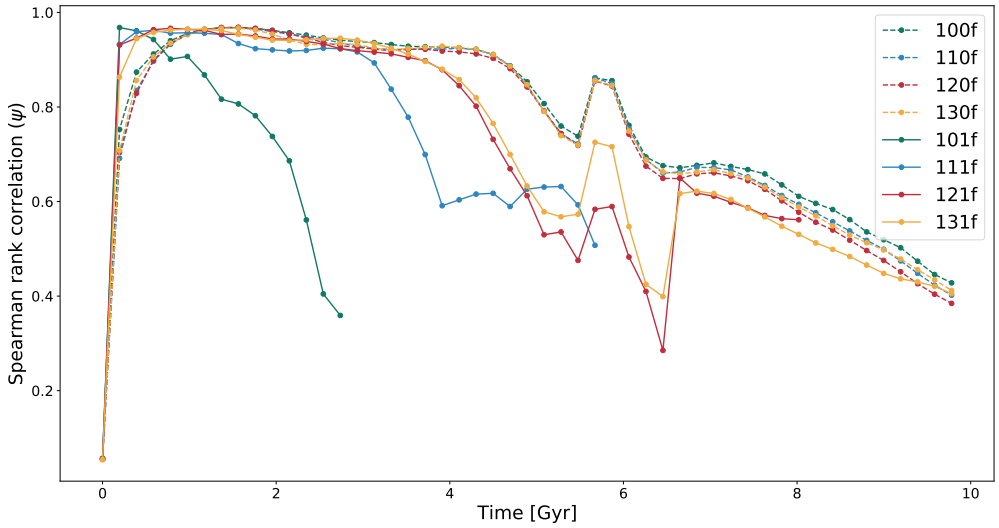

Figure 3.20: Freefall Trajectory: Spearman rank correlation coefficient for gas density and total phase space separation (δ) between shadow runs. Solid lines indicate cooling-on runs and dashed cooling-off. We see a similar trend in loss of correlation with cooling rate as the parabolic suite.

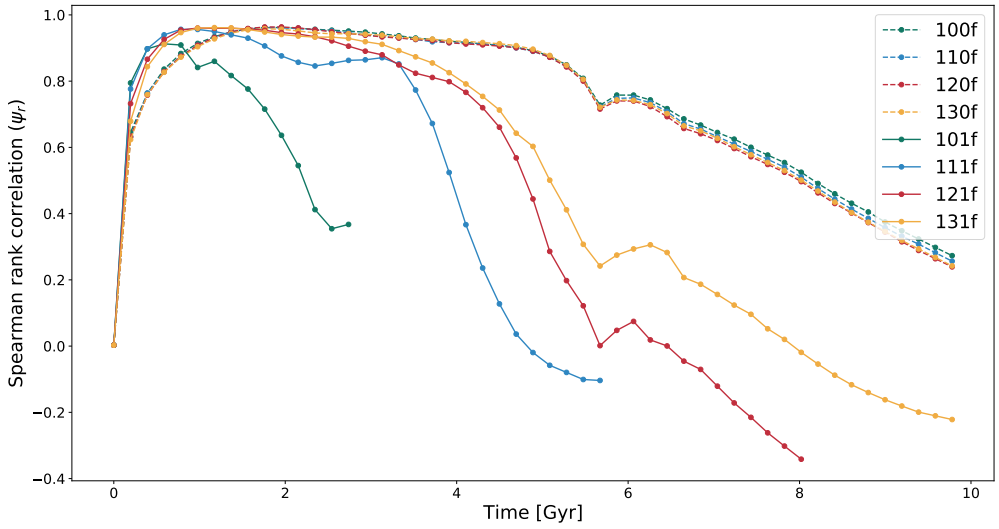

Figure 3.21: Freefall Trajectory: Spearman rank correlation coefficient for gas density and position phase space separation (δ_r) between shadow runs. Solid lines indicate cooling-on runs and dashed cooling-off. Interestingly, 121f and 131f have begin to anti-correlate which is in contrast with parabolic runs.

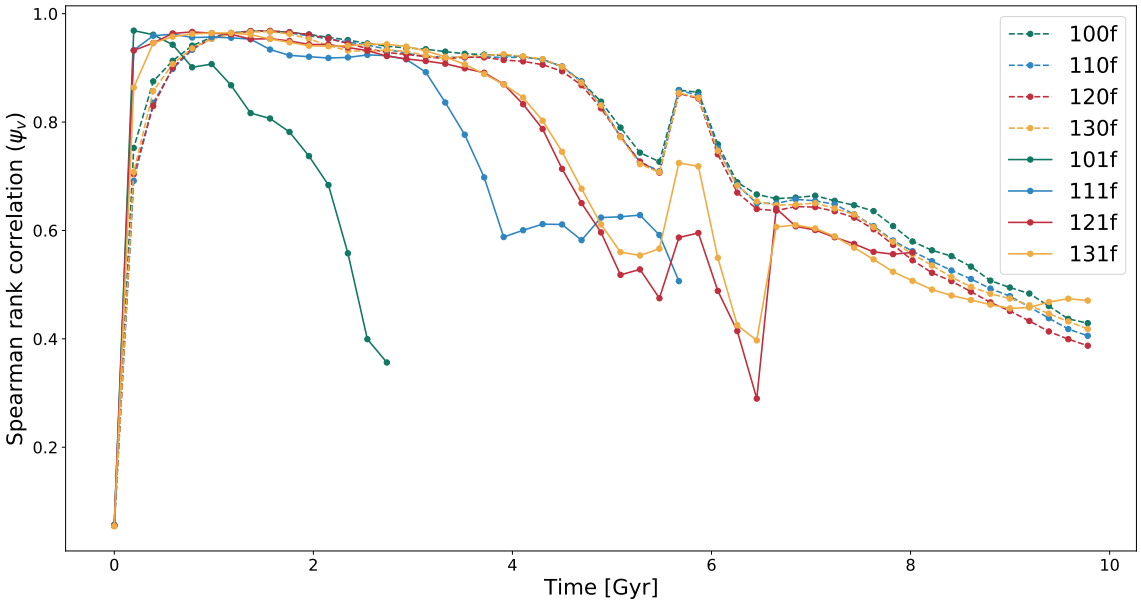

Figure 3.22: Freefall Trajectory: Spearman rank correlation coefficient for gas density and velocity phase space separation (δ_v) between shadow runs. Solid lines indicate cooling-on runs and dashed cooling-off.

3.5 Additional supplemental analyses

While the previous sections give the bulk of the physical insight, we have also analyzed a number of physical parameters in the simulation to test both accuracy and the impact of additional numerical factors, such as changing the position of the perturbation, softening lengths (see appendix A) and angular/linear momentum conservation or lack thereof.

3.5.1 Location of Perturbation

As noted in the introduction there is no single Lyapunov exponent for a systems evolution, technically a large spectrum of them exists associated with perturbations along each degree of freedom. Hence in this section we make a brief exploration of changing the position of the

initial perturbation to examine its impact on the density-phase space separation correlation.

For this suite of simulations, the location of the perturbed particle was varied to measure its impact on the $\rho - \delta$ correlation. Figures 3.23, 3.24, and 3.25 show the results of this experiment. It is clear that the location of perturbation has a less significant impact on the later time evolution (after periapsis), but there are still small differences. At earlier times, however, $100\mathrm{p}_{\mathrm{center}}$ has considerably stronger correlation, although the differences do not follow an obvious behaviour since the next highest correlation is for $100\mathrm{p}_{\mathrm{edge}}$.

Figures 3.26 - 3.28 show the evolution of phase space separations. Here as well, there does not seem to be a trend with location. There are minor differences in the early and late epochs, although interestingly they all agree at periapses (2.93 Gyr). Importantly we conclude that differences caused by cooling are larger than those we observe here. However, it looks like choosing different initial perturbations can induce small changes.

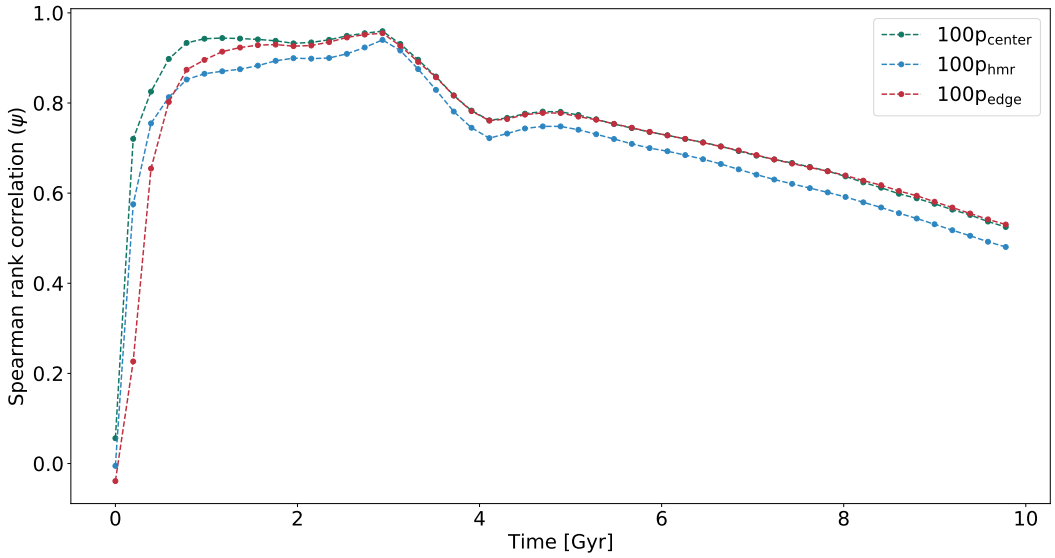

Figure 3.23: Location of Perturbation: Spearman rank correlation coefficient for gas density and total phase space separation (δ) between shadow runs. A trend is apparent only in the first Gyr. Regardless of where the perturbation was applied, overall behavior remains largely similar.

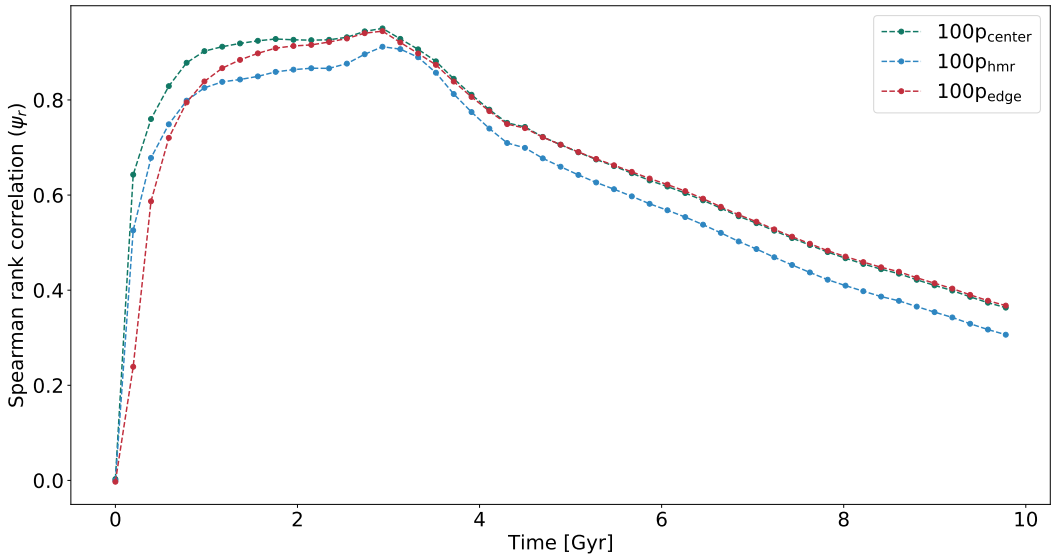

Figure 3.24: Location of Perturbation: Spearman rank correlation coefficient for gas density and position phase space separation (δ_r) between shadow runs. There is a steady decline post-merger.

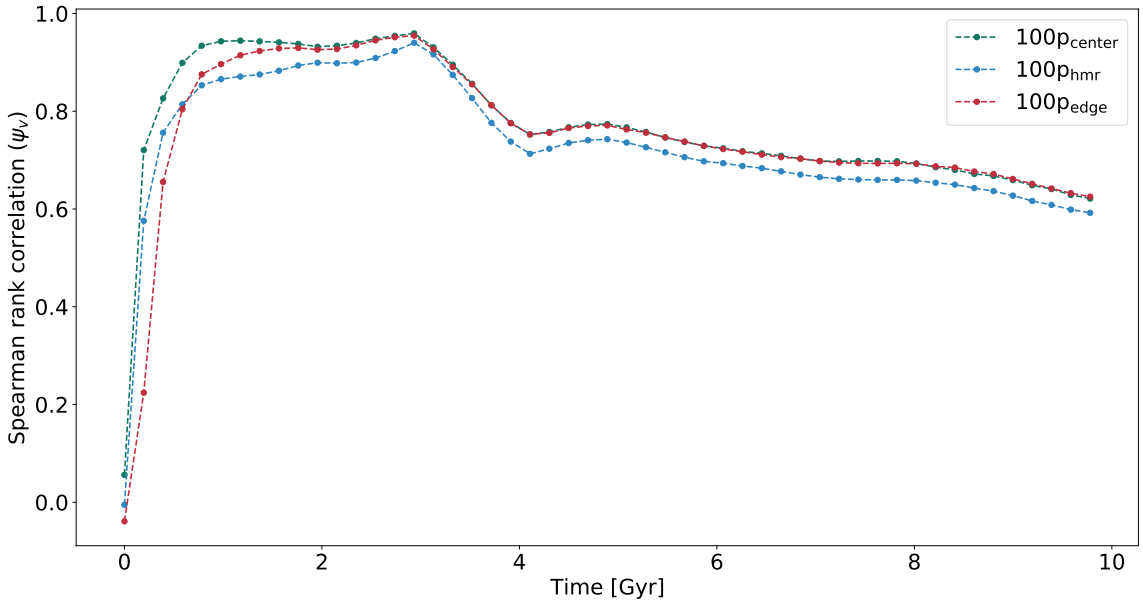

Figure 3.25: Location of Perturbation: Spearman rank correlation coefficient for gas density and velocity phase space separation (δ_v) between shadow runs. Notice the flattening post-merger.

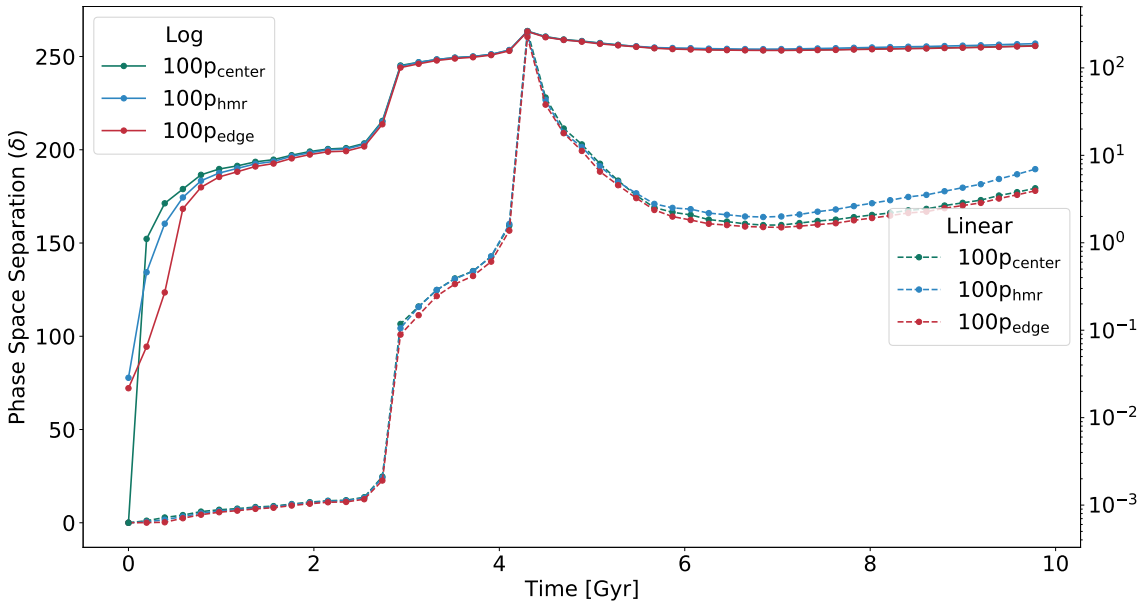

Figure 3.26: Location of Perturbation: Time evolution of the total phase space separation (δ) between shadow runs. Log and linear scales are both shown to visualize early and late term evolution.

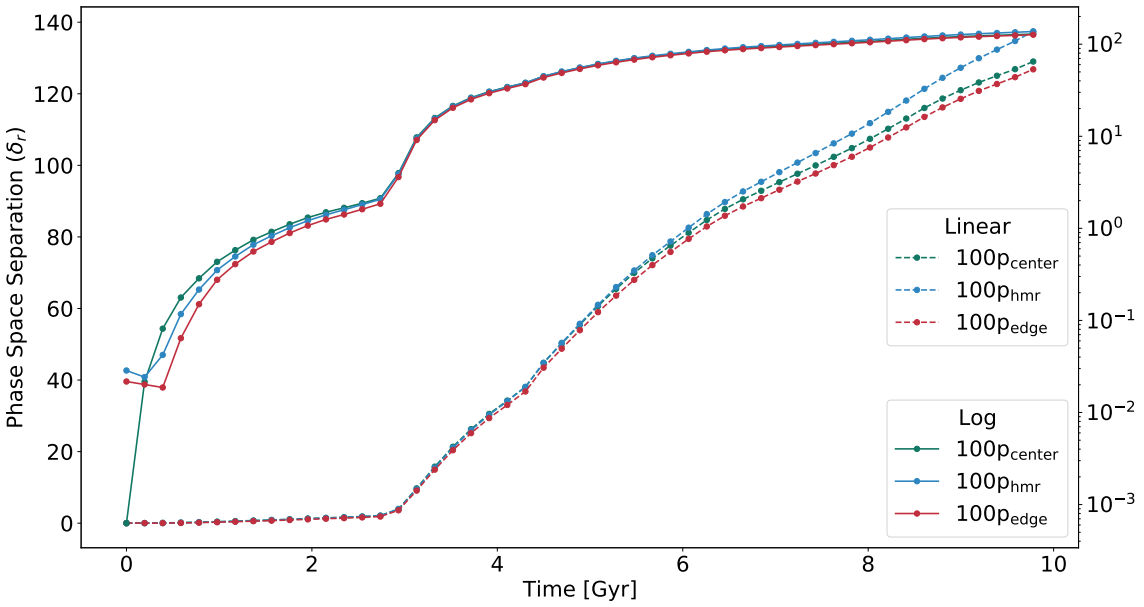

Figure 3.27: Location of Perturbation: Time evolution of the position phase space separation (δ_r) between shadow runs.

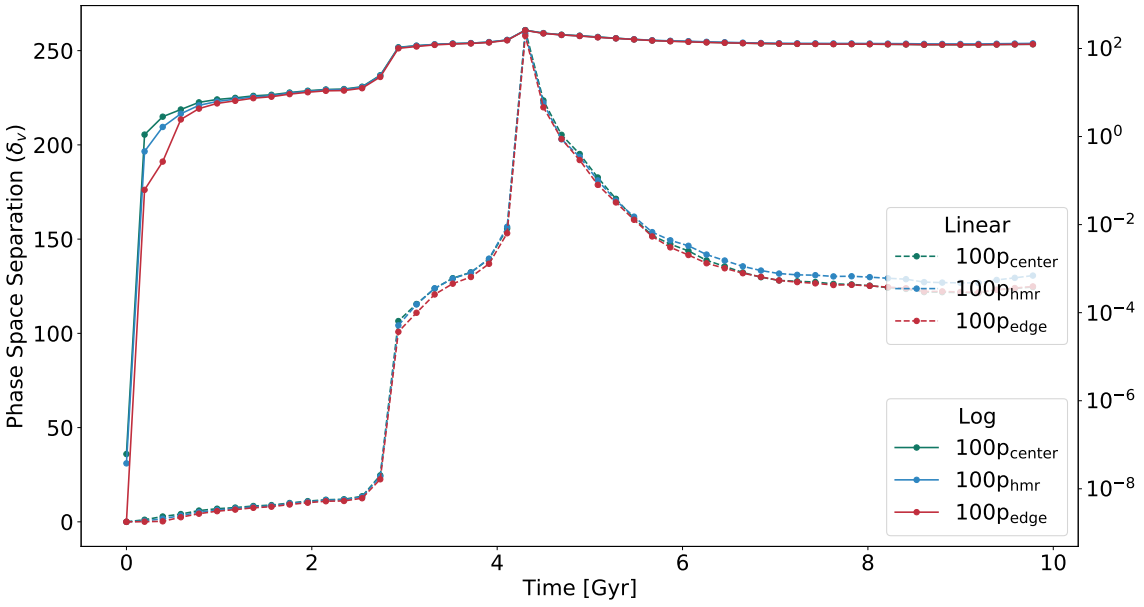

Figure 3.28: Location of Perturbation: Time evolution of the velocity phase space separation (δ_v) between shadow runs.

3.5.2 Angular Momentum Evolution

Angular momentum conservation is a useful test of robustness for simulations, and tree codes are known to not conserve angular momentum. Most of our parabolic simulations exhibit less than 5% change in the total angular momentum of the system. However, two runs have unusual gains in momentum; 101p right from the onset (figure 3.29) and 111p after the merger has completed (figure 3.31). 101p and 111p were terminated at 3.13 and 7.73 Gyr respectively due to poor conservation of angular momentum. Figures 3.29 and 3.30 show a breakdown of contribution from dark matter and gas individually. Although not noticeable in these figures, there is an angular momentum transfer occurring between dark matter and gas, while the total is largely conserved for most runs in the parabolic suite. No freefall cooling-on runs (figure 3.32) on the other hand, conserve angular momentum.

Figures 3.29 - 3.32 also show an interesting trend where the gain in angular momentum is proportional to the mass of the galaxies; 101p, 101f have the highest gain while 131p, 131f have the lowest. This aligns with the trend in cooling rate with mass (101p: shortest cooling time, 131p: longest cooling time). Cooling-off runs conserve angular momentum down to $<1\%$ error which suggests that the errors arising in cooling-on runs are likely due to cooling.

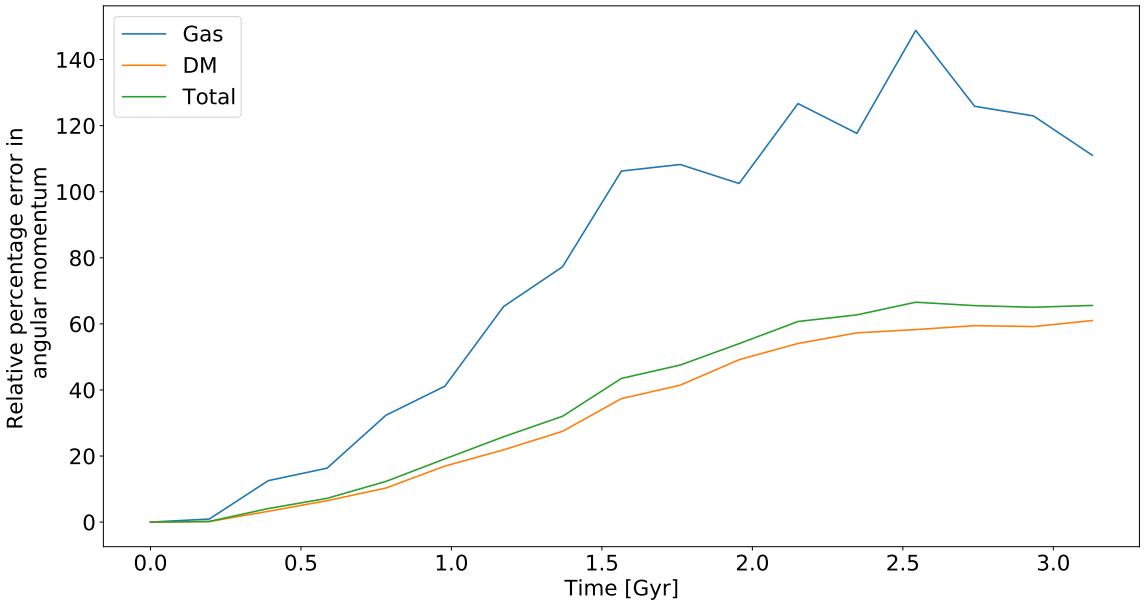

Figure 3.29: Percentage error in the angular momentum over time for 101p. Total angular momentum of the system about center of mass is not conserved. Although, it does appear to plateau, we do not have any further data for this run to comment.

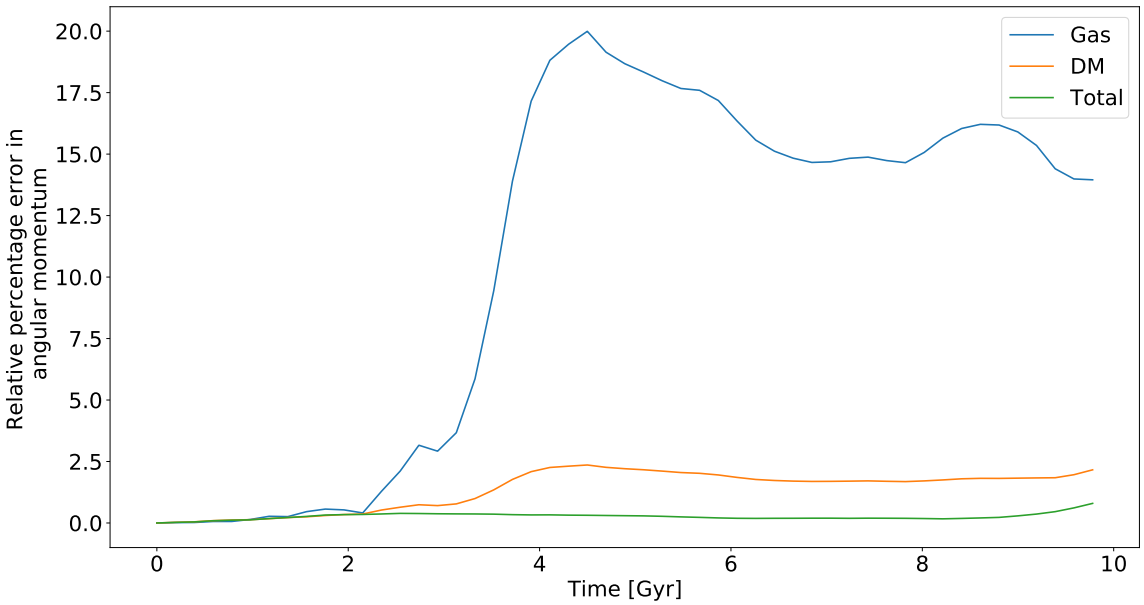

Figure 3.30: Percentage error in the angular momentum over time for 100p. Non-cooling runs conserve angular momentum with less than 2 percent error.

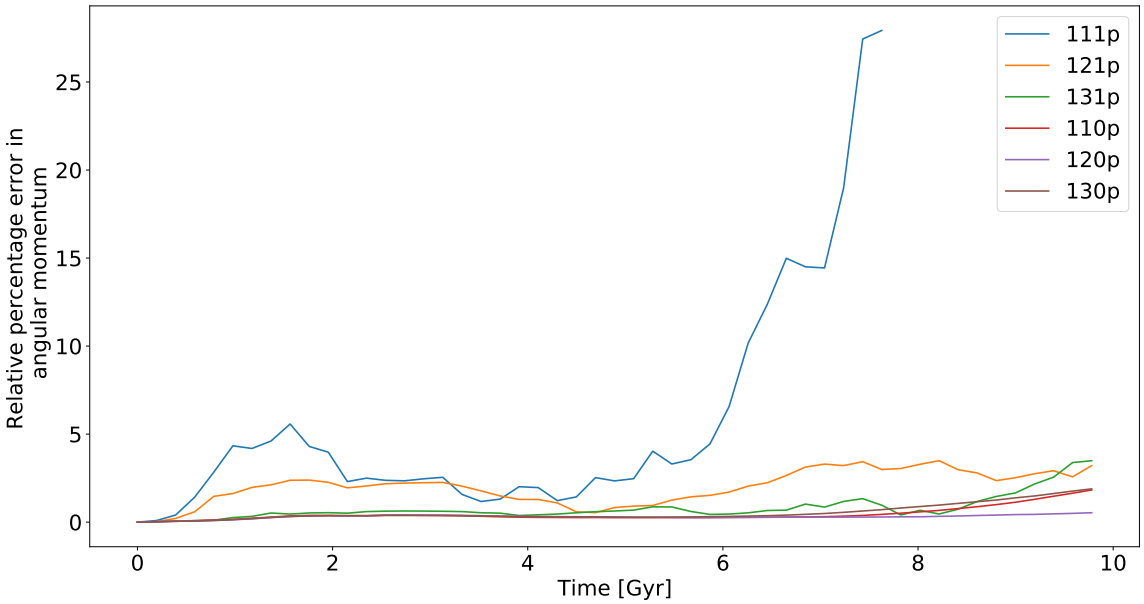

Figure 3.31: Percentage error in the angular momentum over time for all of the parabolic runs. With the exception of 111p which gains a significant amount of angular momentum, although only post-merger, all of the rest are within an acceptable range.

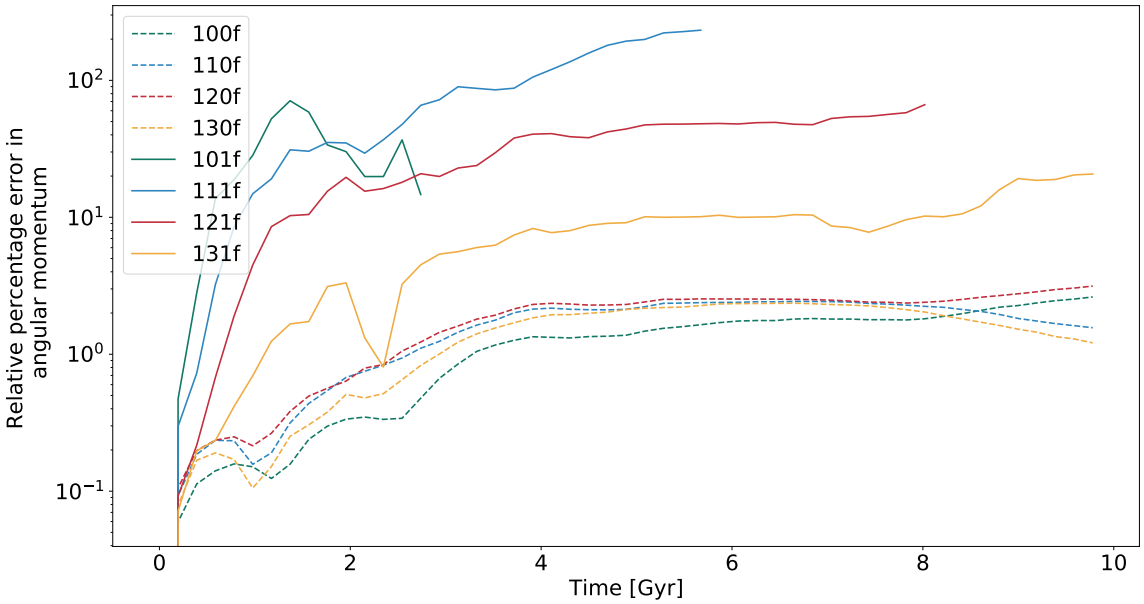

Figure 3.32: Percentage error in the angular momentum over time for all of the freefall runs. Cooling runs have a significant gain in total angular momentum from the onset.

3.5.3 Linear Momentum Evolution

A test of linear momentum conservation was also performed by analyzing the position of system centre of mass over time. Interestingly, the centre of mass was accelerating along the collision axis, the reason for which was later determined to be the positioning of the simulation box centre. All runs analyzed for phase space behaviours are centred with the coordinate origin coinciding with the centre of one of the halos. The asymmetry around the centre could be the cause of such high errors in momentum. We performed test runs for the highest mass systems where the system is centred at the centre of mass. The problem was largely alleviated by this correction as seen in Figure 3.33. Left panels show the position of centre of mass for 131p where the initial conditions box is centred at origin, while the right panels show the same for 131p centred initially at centre of mass. There is at least a 33% difference between these runs in the collision plane, and a lot more in the plane perpendicular.

However, it is worth noting that both simulation pairs showed similar behaviours suggesting that this drift was effectively cancelled out by doing pairwise analyses. We also found that regardless of box centering, the $\rho - \delta$ correlation and phase space separations remains largely unaffected. We have shown comparison plots of origin centred 131p and centre of mass centred 131p in Figure 3.34.

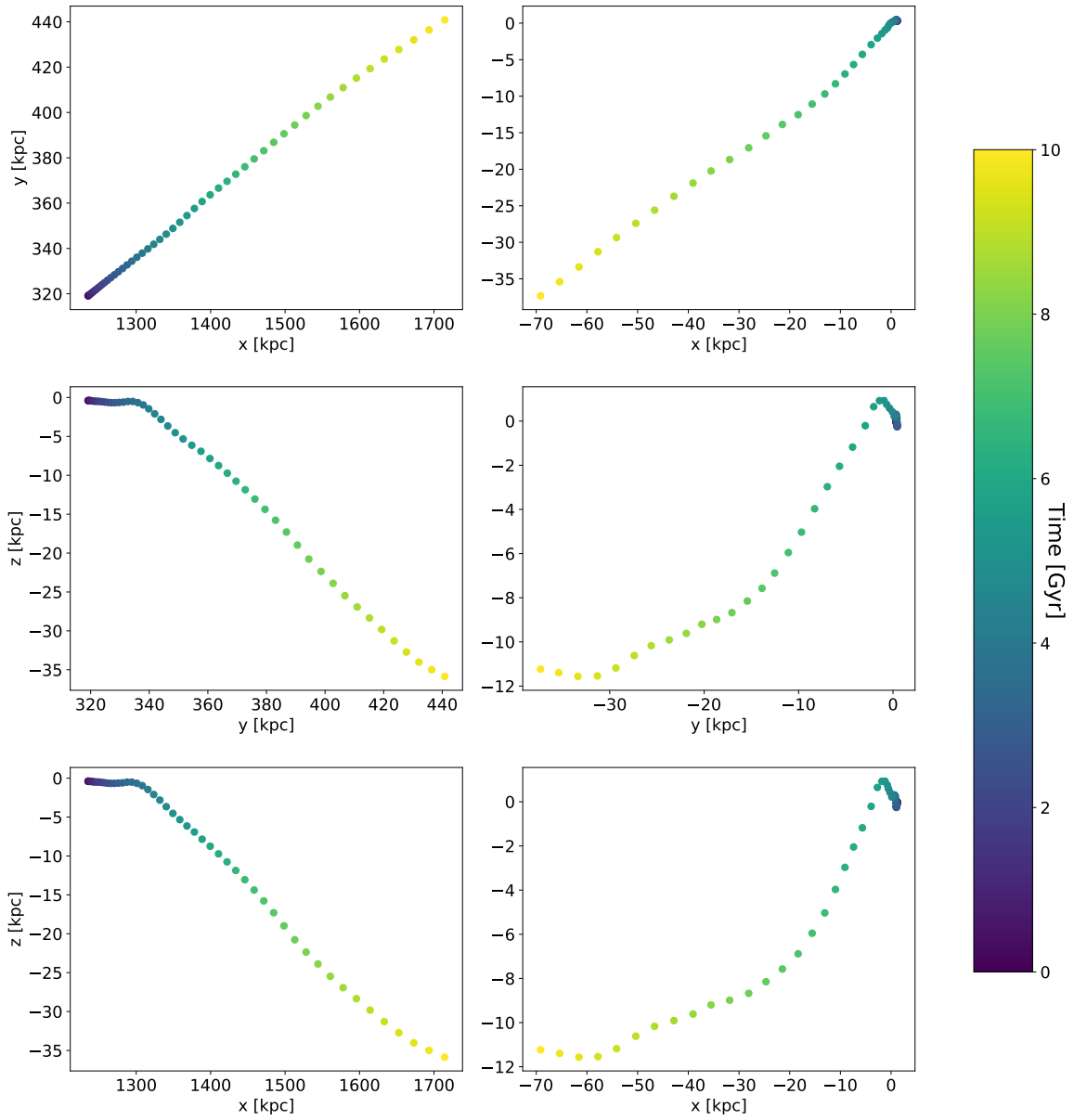

Figure 3.33: Left panels show the change in position of centre of mass for 131p where the initial conditions box is centred at origin, while the right panels show the same for 131p centred initially at centre of mass. Note the significant difference in scales in the x-y plane.

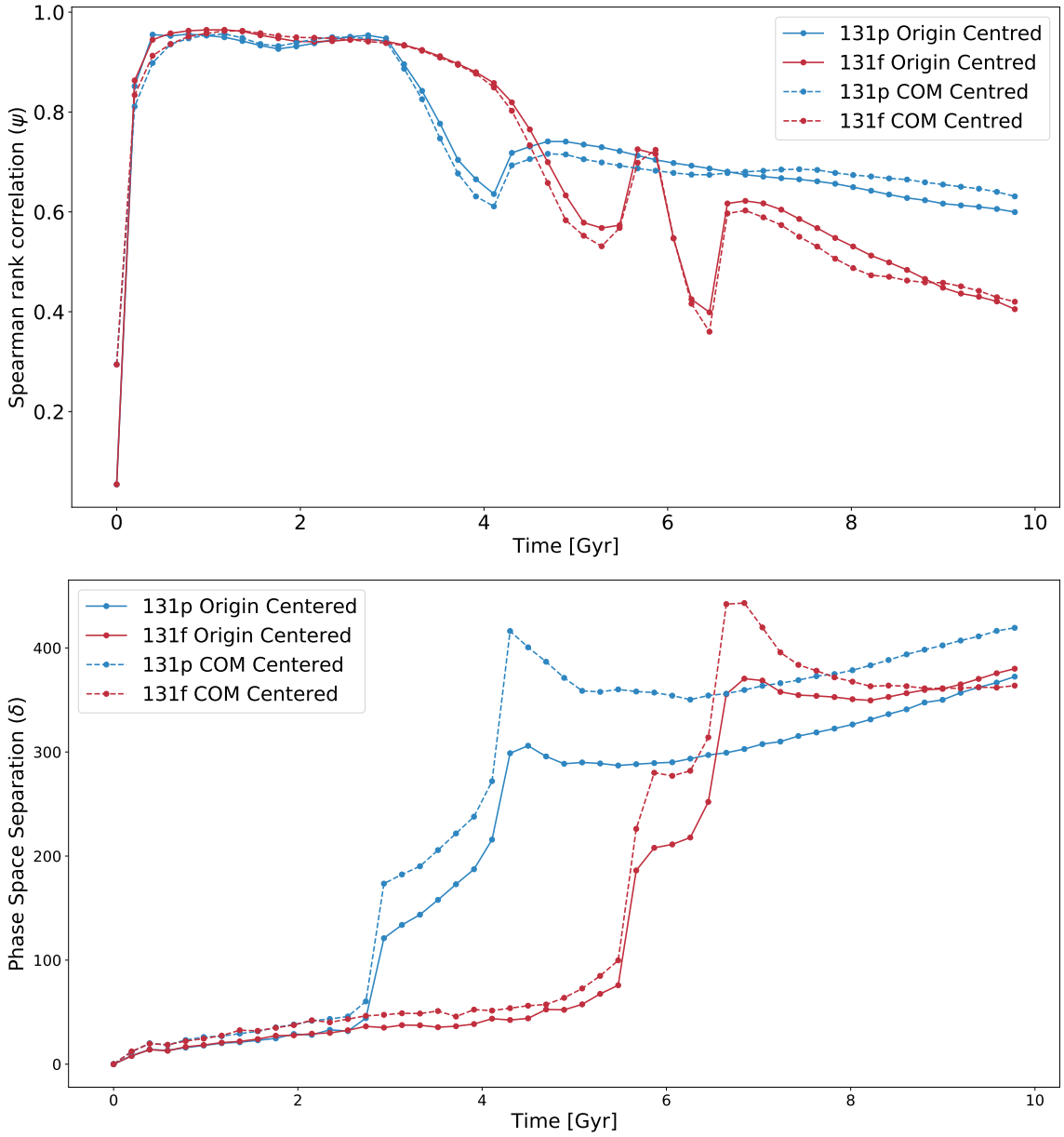

Figure 3.34: Top Panel: Spearman rank correlation coefficient for gas density and total phase space separation (δ) for the original run with the simulation box centred at the origin (centre of one of the halos in the system) and a test run centred at the centre of mass. There is a negligible difference in the correlation, with a significant improvement in the linear momentum conservation of the system. Angular momentum conservation showed improvement only in the parabolic run. Bottom Panel: Evolution of the total phase space separation separations between the origin centered run and centre of mass centred run. Again, there is a difference during the merger, but overall they have similar behavior.

Chapter 4

Discussion

Broadly speaking our analysis has focused on three distinct explorations: Firstly examining how global phase space separation develops, secondly how this relates to changes in local behaviours and lastly whether there are distinct correlations between physical quantities and the local differences.

Our results show that a merger event is a considerably more complex evolutionary event than following mature disk evolution such as in Fields (2019). There are distinct epochs in the phase space evolution, a rapid phase in the beginning and slower post-merger evolution due to approaching virial equilibrium. Since the evolution is faster in parabolic runs because of higher initial interaction velocity, differences in phase space evolution are more noticeable there. Pre-merger time scales are important since they differentiate similar mass systems by the amount of cooling that occurs before processes such as merger shocks start to dominate. Over the entire simulation, we observe that freefall runs with cooling have shorter doubling times than their parabolic counterparts. Post merger, freefall cooling-on runs have shorter

doubling times than parabolic simply because parabolic runs have had a longer time to reach equilibrium and have effectively reached equilibrium while freefall runs will require more time.

For runs with cooling, there is a steep trend in Lyapunov exponent (and doubling time) with galaxy mass, which affirms our conclusion that cooling makes simulations increasingly susceptible to variations in evolution. Cooling off runs, across the board have no significant trend in Lyapunov exponent with mass. It goes to show how cooling can complicate phase space evolution, with processes like accretion shocks significantly increasing the difficulty of maintaining similar evolutionary behaviours.

The net take-away of these results is that we should understand that the development of phase space separations follows distinctly different patterns depending on the stage of the merger. This is analogous to what we see with local weather, depending on local pressure differences weather patterns can be more or less predictable. Adding additional angular momentum complicates evolution by producing a final state with more spin and therefore the possibility of larger velocity differences.

It is evident from the phase space evolution that, mergers are sufficiently non-linear with high (inferred) Lyapunov exponents during certain parts of their evolution. How these differences develop is complex. The fractional distributions of position, velocity and total separations at different epochs of the merger provide hints of how things develop. Pre-merger, separations grow rapidly and the distributions are skewed towards larger values from a small number of particles. Post-merger, the relative distributions begin to converge as virial equilibrium is approached. This sort of behaviour is observed in all runs, cooling-on

and off. They expectedly differ however in the magnitude of separations, since with cooling, gas goes through additional evolutionary stages. Another notable feature in the cooling-on runs (freefall and parabolic) is that, particles in the cold cores have achieved most of their total separation early in the simulation. This gas in the cold phase has limited position and velocity freedom, and thus cannot evolve much further. However, if more realistic feedback were to be present, we can expect differences to grow further in these high density regions as they would be driven by high energy events, such as supernovae. The key conclusion from looking at phase space separation distributions is that, although initially a small fraction of gas contributes towards the change in overall state of the system, at later times, variances grow in all of the material.

One of key drivers of this exploration was to analyze the effect of adding radiative cooling. Our initial hypothesis was that since cooling increases the numerical difficulty of integration and it is dependent on density, we should see high density regions getting separated in phase space from their perturbed shadow simulations, more so than the low density regions.

To test this hypothesis we used Spearman rank correlation to follow the relation between gas density and phase space separations. We found that, while it is true that high density regions can develop large phase space separations, especially at the beginning of the simulation, the long term evolution of a merger is more complex. There are physical processes at work, in particular propagation of shocks which usually tend to move from high density to low, and their interplay with cooling produces non-trivial behaviours. For these simulations we find differences actually percolate throughout the simulation volume and that there is not a simple correlation between phase space separation and density.

During early epochs if the gas has enough time to cool, correlations were observed to be dropping in both the freefall and parabolic runs. The onset of cooling at the beginning of the simulation produces a weak accretion shock, which occurs when gas infalling at supersonic velocities is breaked by more slowly infalling or stationary gas. As the radius at which cooling is important increases with time, this generally results in the shock front increasing in radius. Since the shock boundary is not characterized by material propagating outwards, but rather a kind of density wave being generated by the slowing of infalling gas, there is no actual transport of gas from high to low density regions. These shocks introduce perturbations at increasingly lower densities and are thus responsible for the growth of separations in lower density regions where normally it would take longer for them to develop.

After the closest approach, a weak merger shock with Mach number ~ 1.5, disperses some of the material from the central high density regions to much larger distances at high velocities. The formation of a merger shock marks the beginning of a significant drop in $\rho - \delta$ correlation. Even though this process occurs in all runs, depending on the amount of cold gas, this decline starts earlier for halos with higher cooling rates. In the parabolic suite, there seems to be a post merger recovery in correlation. There is no apparent trend with mass in this behaviour though. Some of the parabolic simulations have developed a cold spiral disk at the center, but there is not enough data for us to claim any connection between disk formation and correlation increase. Freefall runs show no sign of such recovery post merger.

Surprisingly the location of the initial perturbation is only slightly important in determining the long term $\rho - \delta$ correlation, with no discernible trend with radius. The only

noticeable trend is how quickly the separations grow and correlate with density in the first Gyr. Expectedly, a perturbation at the edge percolates slower throughout the distribution than ones at half mass radius and center. It would be interesting and informative to perform a similar analysis with the presence of radiative cooling.

Lastly, the lack of angular momentum conservation and movement of the center of mass is concerning from an accuracy perspective, although we note that since both simulations have the same issue the phase space analysis does tend to subtract out drifts in the centre of mass, for example. There is non-trivial run to run variation as well at later times in both parabolic and freefall. However, this variance was negligible in our test runs with the simulation box initially centered at the center of mass of the system. It also seemed to perform better in angular momentum conservation, although only in the parabolic run. Center of mass also shows a much better restraint in movement across the collision axis in both freefall and parabolic runs. Nonetheless, as noted, this issue does not affect our results because of the comparative nature of our analysis, but one needs to be wary of additional errors this may generate.

Chapter 5

Conclusions

We have presented an analysis of the evolution of phase space separations for identical initial conditions with a minor perturbation. Our goal being to both measure the separations and determine whether they could be easily related to local changes and/or physical quantities.

Different phases of a merger have different characteristic timescales, which is complicated further by choice of the initial approach velocity and angular momentum. Thus having a single Lyapunov exponent for the entire merger does not characterize well the phase space separation evolution. As seen in the results section, Lyapunov exponents vary depending on the epoch; the post merger exponent is considerably smaller than the overall simulation, but looking only at the overall exponent, we miss the complexity of merger processes.

Our principle conclusions are:

- The addition of radiative cooling makes nearly identical runs separate in phase space much faster than without cooling. As we go to lower masses, cooling times get shorter

and consequently, the evolution of phase space separations is faster.

- By applying physical scaling to produce different mass systems, we recovered strongly similar behaviours in runs without cooling.

- Although the shocks we noticed, both accretion and merger driven, were low Mach number, they have the potential to introduce differences throughout the simulation volume.

- Taken together, both cooling and shock processes lead to differences throughout the simulation volume and, importantly these differences can change throughout the merger evolution.

- We also found that density can correlate poorly with phase space separations. Runs with cooling tend to lose any initial correlation even before merger dynamics has a chance to introduce further differences, although there is a dependence on the halo mass. Non-cooling runs also exhibit a decline in correlation post merger due to virialization, albeit slowly. Hence, our hypothesis that, with cooling, high-density regions should have more separations than low density regions has been shown to breakdown, especially at later times during the merger.

In this thesis, using a combination of phase space analysis and $\rho - \delta$ correlation, we have put forward an analysis of challenges arising from minute perturbations in simulations of structure formation. We showed that these small variances can and do affect the entire simulation volume in many cases. Given the limited amount of computational resources available

currently, approximations are unavoidable, but understanding their impact in gravity and hydrodynamic simulations is of great importance.

5.1 Future Work

The next logical step in this analysis is to look at more realistic galaxies/halo models. Including substructure is an important next step that is missing from this analysis. It would also be useful to look at the effects of gravity solvers as these have a major influence on both accuracy and conservation properties. A comparison with an ideal exact solver ("N^2") would help us assess the role of approximations in gravity calculations. Hydrodynamics, on the other hand, will always be subject to elements of approximation, although a code comparison have proven to be useful in the past.

Finally, more complex physics modules such as star formation and feedback should be examined especially as these process are non-reversible. With the presence of heating from localized high energy feedback from supernovae or black holes, it would not be surprising if differences grow quicker and are stronger.

Bibliography

Balaji, P. & Kimpe, D. 2013, in 2013 IEEE 10th International Conference on High Performance Computing and Communications 2013 IEEE International Conference on Embedded and Ubiquitous Computing, 407–414

Barnes, J. & Hut, P. 1986, Nature , 324, 446

Barnes, J. E. 1988, ApJ , 331, 699

Bate, M. R. & Burkert, A. 1997, MNRAS , 288, 1060

Benson, A. J. 2010, Phys. Rep. , 495, 33

Blumenthal, G. R., Faber, S. M., Primack, J. R., & Rees, M. J. 1984, Nature , 311, 517

Booth, C. M. & Schaye, J. 2009, MNRAS , 398, 53

Bourne, M. A., Zubovas, K., & Nayakshin, S. 2015, MNRAS , 453, 1829

Cavaliere, A. & Fusco-Femiano, R. 1976, A&A , 500, 95

Cox, T. J., Jonsson, P., Primack, J. R., & Somerville, R. S. 2006, MNRAS , 373, 1013

Dzyuba, B. M. & Yakubov, V. B. 1970, Soviet Ast. , 14, 1

Efstathiou, G. & Silk, J. 1983, Fundamentals of Cosmic Physics, Vol. 9

Eggen, O. J., Lynden-Bell, D., & Sandage, A. R. 1962, ApJ , 136, 748

Farouki, R. T. & Shapiro, S. L. 1982, ApJ , 259, 103

Fields, T. 2019, Master's thesis, Saint Mary's University

Genel, S., Bryan, G. L., Springel, V., et al. 2019, ApJ , 871, 21

Gerhard, O. E. 1981, MNRAS , 197, 179

Gingold, R. A. & Monaghan, J. J. 1977, MNRAS , 181, 375

Goldstein, H., Poole, C., & Safko, J. 2002, Classical mechanics (Addison Wesley)

Gott, J. R., I. & Thuan, T. X. 1976, ApJ , 204, 649

Gott, J. Richard, I. 1975, ApJ , 201, 296

Gott, Richard J., I. 1973, ApJ , 186, 481

Green, S. B. & van den Bosch, F. C. 2019, MNRAS , 490, 2091

He, Y. & Ding, C. H. 2001, The Journal of Supercomputing, 18, 259

Henon, M. & Heiles, C. 1964, AJ , 69, 73

Hernquist, L., Hut, P., & Makino, J. 1993, ApJ , 402, L85

Hockney, R. W. & Eastwood, J. W. 1988, Computer simulation using particles (CRC Press)

Hohl, F. & Zang, T. A. 1979, AJ , 84, 585

Hopkins, P. F. 2015, MNRAS , 450, 53

Hopkins, P. F., Grudić, M. Y., Wetzel, A., et al. 2020, MNRAS , 491, 3702

Hopkins, P. F., Kereš, D., Oñorbe, J., et al. 2014, MNRAS , 445, 581

Hopkins, P. F., Wetzel, A., Kereš, D., et al. 2018, MNRAS , 480, 800

Hubble, E. 1926, Contributions from the Mount Wilson Observatory / Carnegie Institution of Washington, 324, 1

Ibarra, A. 2015, Nuclear and Particle Physics Proceedings, 267-269, 323

Kandrup, H. E. & Smith, Haywood, J. 1991, ApJ , 374, 255

Kaufmann, T., Mayer, L., Wadsley, J., Stadel, J., & Moore, B. 2007, MNRAS , 375, 53

Kay, S. T., Pearce, F. R., Frenk, C. S., & Jenkins, A. 2002, MNRAS , 330, 113

Keller, B. W., Wadsley, J. W., Wang, L., & Kruijssen, J. M. D. 2019, MNRAS , 482, 2244

Kimock, B., Narayanan, D., Smith, A., et al. 2020, arXiv e-prints, arXiv:2004.08397

Kuijken, K. & Dubinski, J. 1995, MNRAS , 277, 1341

Larson, R. B. 1974a, MNRAS , 166, 585

Larson, R. B. 1974b, MNRAS , 169, 229

Larson, R. B. 1975, MNRAS , 173, 671

Larson, R. B. 1976, MNRAS , 176, 31

Lucy, L. B. 1977, AJ , 82, 1013

Lupi, A., Volonteri, M., & Silk, J. 2017, MNRAS , 470, 1673

Marri, S. & White, S. D. M. 2003, MNRAS , 345, 561

McCarthy, I. G., Schaye, J., Bird, S., & Le Brun, A. M. C. 2017, MNRAS , 465, 2936

Mihos, J. C. & Hernquist, L. 1996, ApJ , 464, 641

Miller, R. H. 1964, ApJ , 140, 250

Miller, R. H. 1978, ApJ , 223, 122

Miller, R. H. & Smith, B. F. 1979a, ApJ , 227, 785

Miller, R. H. & Smith, B. F. 1979b, ApJ , 227, 407

Mo, H., Bosch, F. V. d., & White, S. 2010, Galaxy formation and evolution (Cambridge University Press)

Moreno, J., Torrey, P., Ellison, S. L., et al. 2020, Monthly Notices of the Royal Astronomical Society

Mróz, P., Udalski, A., Skowron, D. M., et al. 2019, ApJ , 870, L10

Park, J., Smith, R., & Yi, S. K. 2017, The Astrophysical Journal, 845, 128

Robertson, B. E. & Kravtsov, A. V. 2008, ApJ , 680, 1083

Rubin, V. C. & Ford, W. Kent, J. 1970, ApJ , 159, 379

Scannapieco, C., Tissera, P. B., White, S. D. M., & Springel, V. 2006, MNRAS , 371, 1125

Schmidt, M. 1959, ApJ , 129, 243

Somerville, R. S. & Davé, R. 2015, ARA&A , 53, 51

Springel, V. 2005, MNRAS , 364, 1105

Springel, V. 2010, MNRAS , 401, 791

Springel, V., Wang, J., Vogelsberger, M., et al. 2008, MNRAS , 391, 1685

Stinson, G., Seth, A., Katz, N., et al. 2006, MNRAS , 373, 1074

Su, K.-Y., Hopkins, P. F., Hayward, C. C., et al. 2018, Monthly Notices of the Royal Astronomical Society, 480, 1666

Sutherland, R. S. & Dopita, M. A. 1993, ApJS , 88, 253

Tasker, E. J. & Bryan, G. L. 2006, ApJ , 641, 878

Thacker, R. J. & Couchman, H. M. P. 2000, ApJ , 545, 728

Thompson, B. 2017, Ph.D., University of Central Lancashire

Toomre, A. & Toomre, J. 1972, ApJ , 178, 623

Truelove, J. K., Klein, R. I., McKee, C. F., et al. 1997, ApJ , 489, L179

van den Bosch, F. C. & Ogiya, G. 2018, Monthly Notices of the Royal Astronomical Society, 475, 4066

Virtanen, P., Gommers, R., Oliphant, T. E., et al. 2020, Nature Methods, 17, 261

Vogelsberger, M., Marinacci, F., Torrey, P., & Puchwein, E. 2020, Nature Reviews Physics, 2, 42

White, S. D. M. 1978, MNRAS , 184, 185

White, S. D. M. & Rees, M. J. 1978, MNRAS , 183, 341

Widrow, L. M. & Dubinski, J. 2005, ApJ , 631, 838

Widrow, L. M., Pym, B., & Dubinski, J. 2008, ApJ , 679, 1239

York, D. G., Adelman, J., Anderson, John E., J., et al. 2000, AJ , 120, 1579

Zhang, T., Liao, S., Li, M., & Gao, L. 2019, MNRAS , 487, 1227

Zhu, Q., Smith, B., & Hernquist, L. 2017, MNRAS , 470, 1017

Appendices

Appendix A

Impact of Softening Length

As a tertiary analysis, that changes aspects of the gravity solver, we looked at how varying softening length impacts the $\rho - \delta$ correlation and phase space separations (Figures A.1-A.3). The values used for softening lengths are presented in 2.6. Cooling was turned off to accurately measure specifically the impact of varying softening lengths. $100\mathrm{p}_{\epsilon=1}$ is the fiducial pair and the sub-script number in other runs show the scaling of softening lengths relative to it.

All four runs are similar at 2 Gyr but before that seem to follow to a trend that the shortest softening length correlates most weakly and largest most strongly. During the merger, however, this behavior reverses while after periapsis, $100\mathrm{p}_{\epsilon=4}$ loses correlation the quickest. However, the overall differences in correlation are small at the end ($\sim 3\%$).

Looking at phase space separations in Figures A.4-A.6, there is a somewhat larger difference among the runs even if the behaviour is largely the same. The trend is not exactly correlated with the softening either as while the largest separation is for the longest soft-

ening length, the smallest separation is for the second smallest softening. Although, the differences at the end are larger here (10%) as compared to the parabolic runs with cooling off at different masses (3.8%). In other words, softening has more influence on overall phase space separations than mass.

In conclusion, the softening length does have an impact, so, as expected, it clearly is a contributing factor in the phase space separations. It would be very informative to perform this analysis with radiative cooling, since softening length directly impacts the maximum possible density and consequently the rate of cooling.

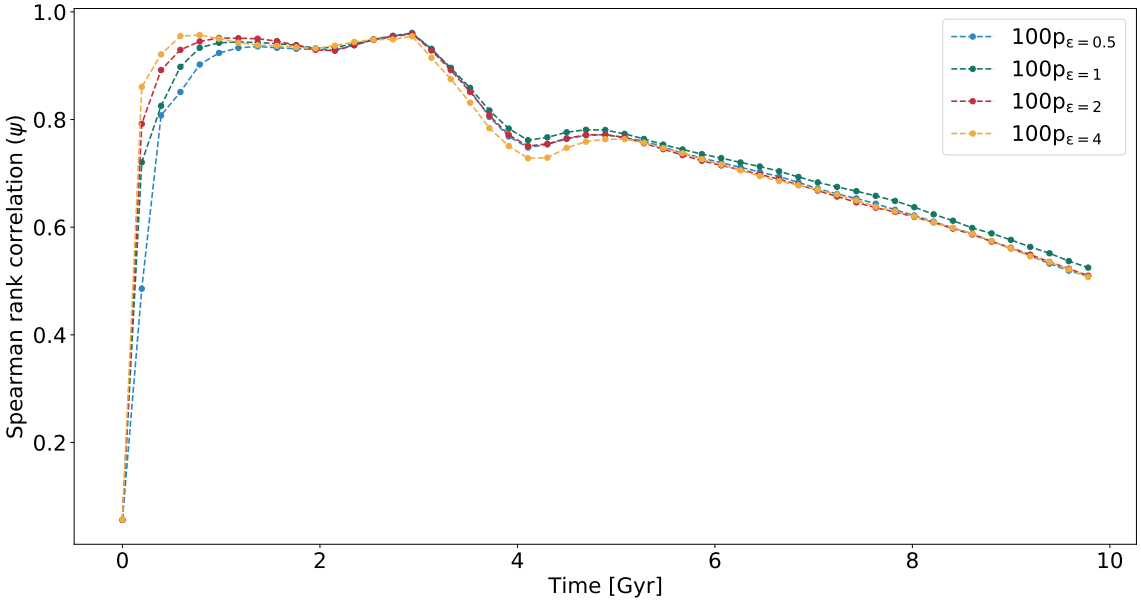

Figure A.1: Softening: Spearman rank correlation coefficient for gas density and total phase space separation (δ) between shadow runs. There is a trend in the first two Gyr and shortly after periapses (2.93 Gyr). Shorter softening lengths appear to correlate slower and also lose it slower. After 5 Gyr, they are virtually indistinguishable.

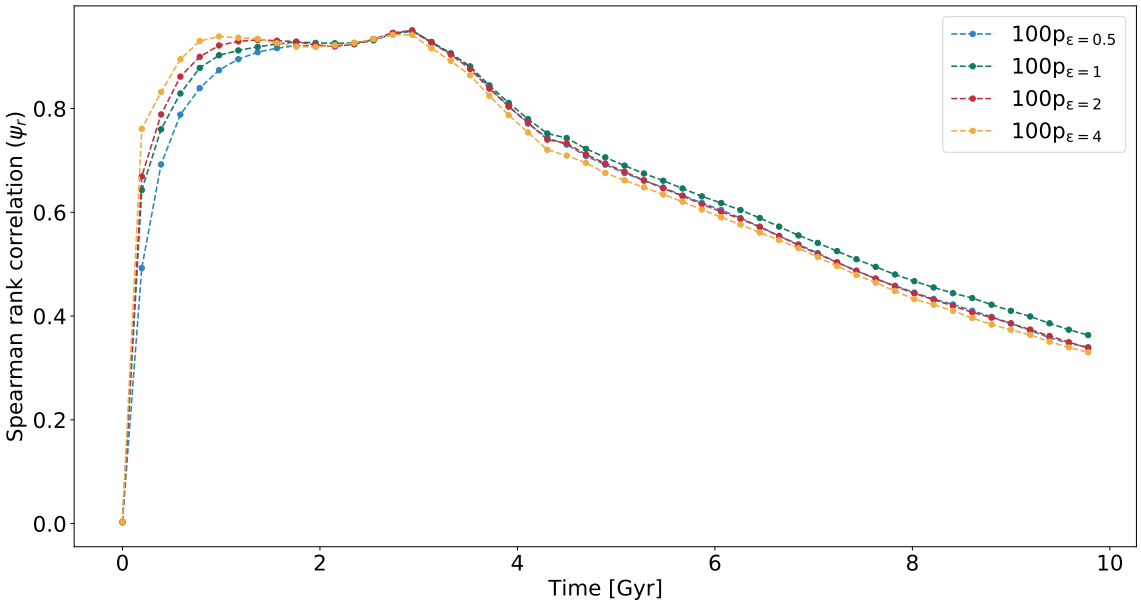

Figure A.2: Softening: Spearman rank correlation coefficient for gas density and position phase space separation (δ_r) between shadow runs. Here the trend is significant throughout the merger.

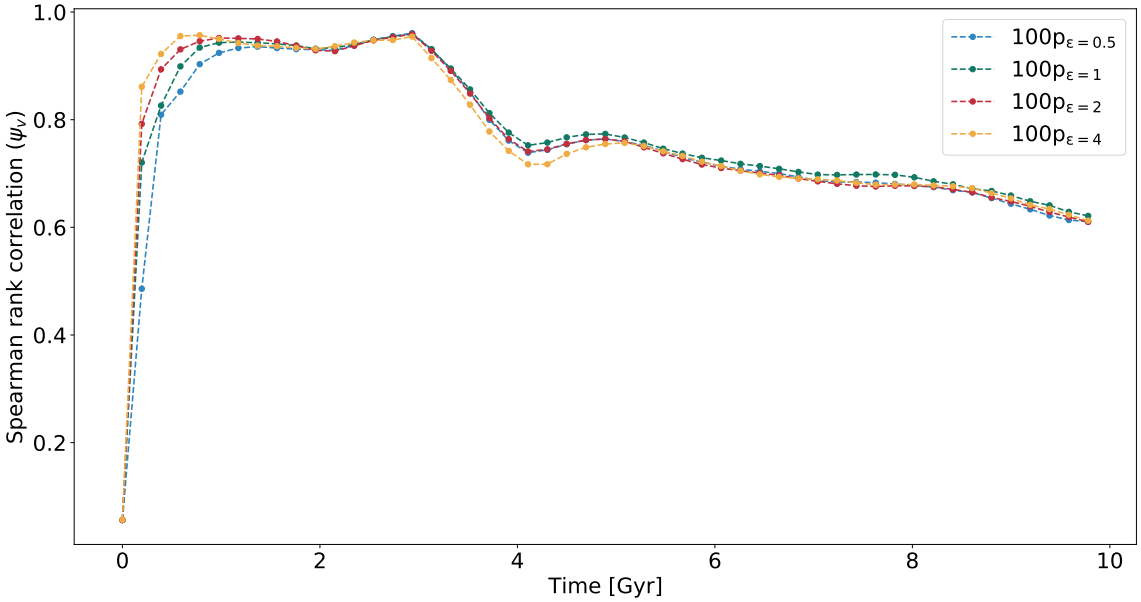

Figure A.3: Softening: Spearman rank correlation coefficient for gas density and total phase space separation (δ_v) between shadow runs.

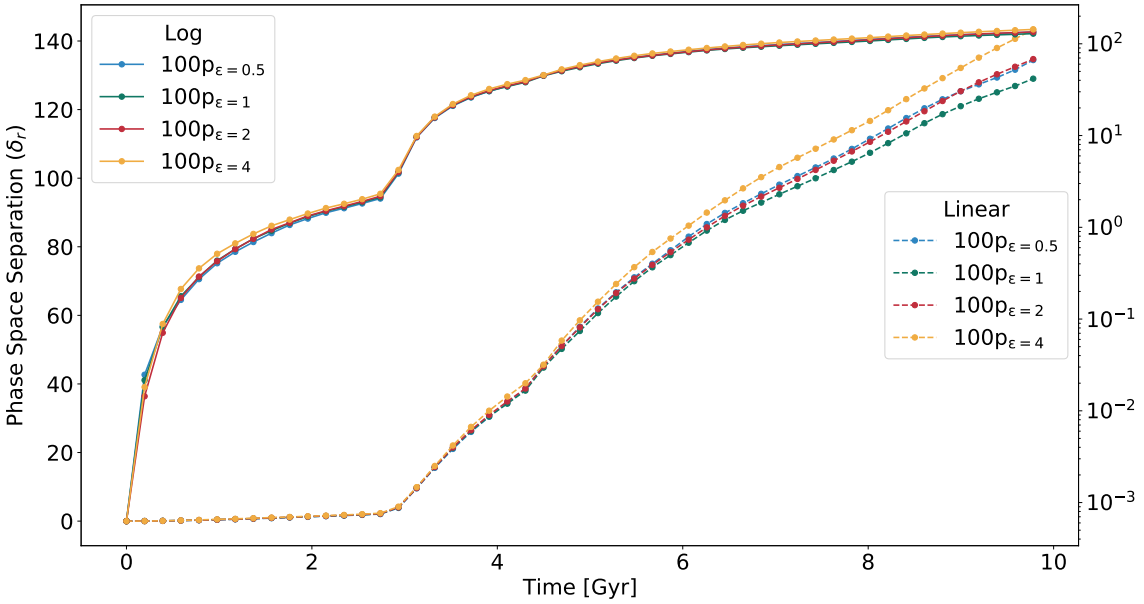

Figure A.4: Softening: Evolution of the position phase space separations (δ_r) between shadow runs in log and linear scales. Note the weak trend at later times where shorter softening lengths separated less.

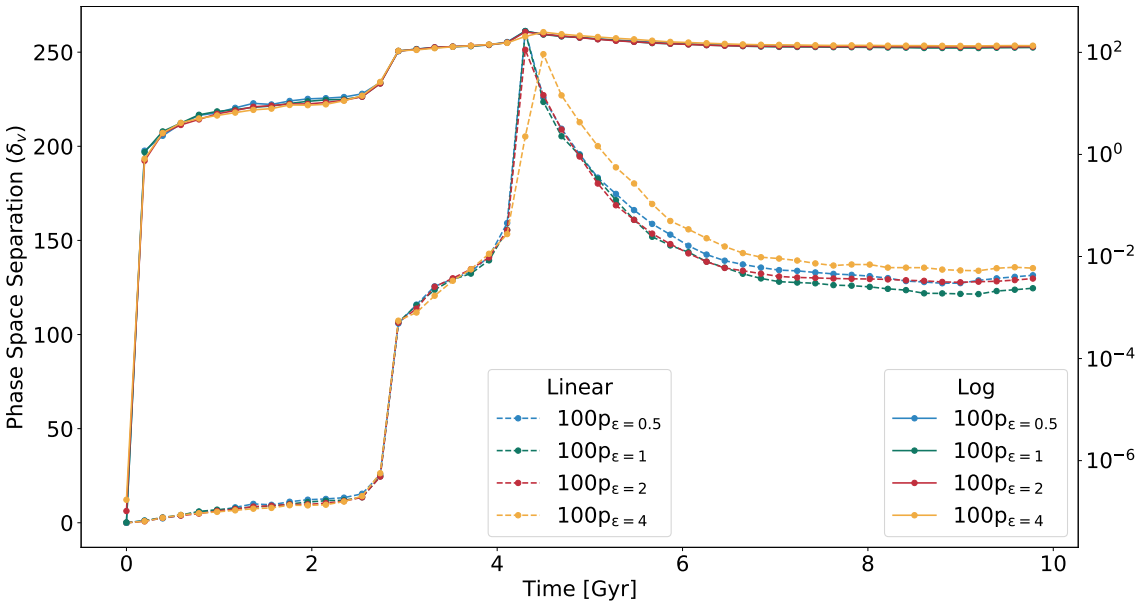

Figure A.5: Softening: Evolution of the velocity phase space separations (δ_v) between shadow runs in log and linear scales. A weak trend similar to the position separations is also visible here. The overall behavior is similar but the magnitudes vary with softening.

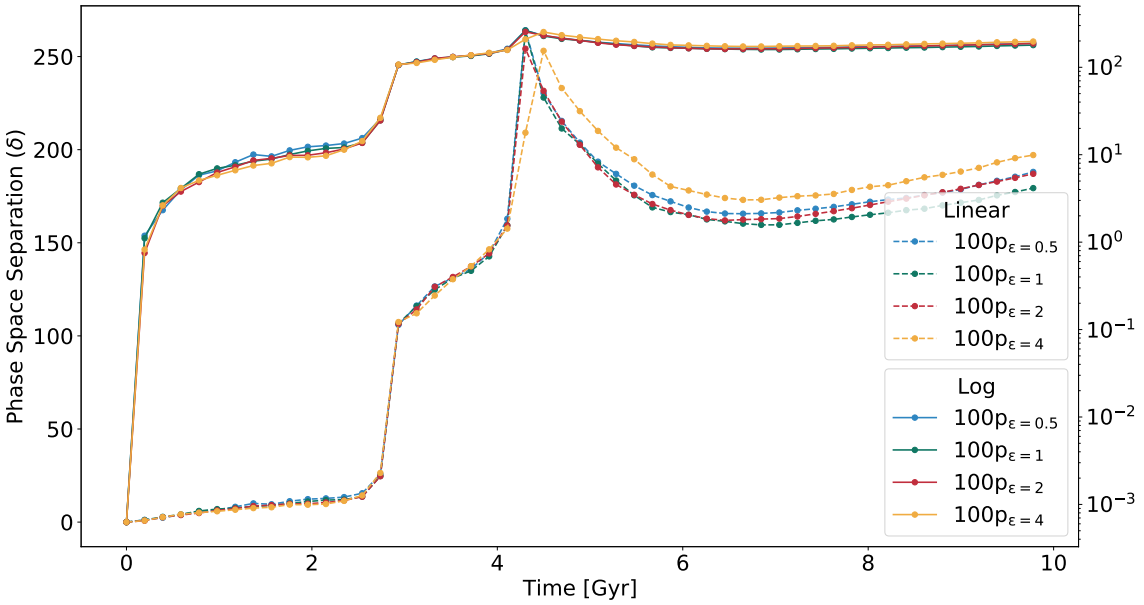

Figure A.6: Softening: Evolution of the total phase space separations (δ) between shadow runs in log and linear scales.